LAWRENCE
LIVERMORE
NATIONAL
LABORATORY

LLNL-TR-679839

DEM Particle Fracture Model

B. Zhang, E. B. Herbold, M. A. Homel, R. A. Regueiro

December 1, 2015

Disclaimer

This work performed under the auspices of the U.S. Department of Energy by Lawrence Livermore National Laboratory under Contract DE-AC52-07NA27344.

Contents

DEM Particle Fracture Model

Boning Zhang[1], Eric B. Herbold[2*],
Michael A. Homel[2], Richard A. Regueiro[1]

[1] *University of Colorado, Boulder, UCB 428, Boulder, CO 80309, USA*
[2] *Atmospheric, Earth and Energy Division, Lawrence Livermore National Laboratory, Livermore, CA 94550, USA * corresponding author*

Abstract

An adaptive particle fracture model in poly-ellipsoidal Discrete Element Method is developed. The poly-ellipsoidal particle will break into several sub-poly-ellipsoids by Hoek-Brown fracture criterion based on continuum stress and the maximum tensile stress in contacts. Also Weibull theory is introduced to consider the statistics and size effects on particle strength. Finally, high strain-rate split Hopkinson pressure bar experiment of silica sand is simulated using this newly developed model. Comparisons with experiments show that our particle fracture model can capture the mechanical behavior of this experiment very well, both in stress-strain response and particle size redistribution. The effects of density and packings of the samples are also studied in numerical examples.

Keywords: Discrete Element Method, particle fracture model, high strain rate, split Hopkinson pressure bar experiments, Hoek-Brown fracture criterion, maximum tensile stress in contacts, packing effects

Acknowledgments

The research performed here was performed in collaboration with Boning Zhang during a summer student intern program at LLNL from his host, Rich Regueiro at University of Colorado, Boulder in 2015. EBH and MAH would like to acknowledge the Joint DoD / DOE Munitions Technology Development Program (JMP) for partial funding to perform this work. EBH is thankful to Jim McCarrick, the JMP Manager at LLNL, for sponsoring this effort. BZ and RAR acknowledge partial funding for this research by ONR MURI grant N00014-11-1-0691.

1 Introduction

It is well known that knowledge of behavior of soils is very important in geotechnical engineering, mining engineering and petroleum engineering. Soil behavior is also important in areas of debris flow, landslides, pavement, and dam construction [Horner et al., 2001, Regueiro et al., 2014]. The mechanical behavior of soils is complicated because of its discrete nature [Zhu et al., 2008]. On the other hand, macroscale behavior of soils results from particle-level interactions [Cho et al., 2006]. Thus, the investigation of soils at multiple scales is necessary to understand their bulk mechanical response. Particle fractures in one-dimensional and triaxial compression experiments have been reported in the literature Vesic and Clough [1968], Yamamuro et al. [1996], Luo et al. [2014a,b, 2011]. The macro-behavior of soils, such as stress-strain path, strength, permeability, are affected by particle fracture, which was observed in Yamamuro et al. [1996], Lade et al. [1996]. The split Hopkinson pressure bar (SHBP) is a widely used experimental approach in studies of compressive behavior of soils at high strain-rate. Using this method, [Kabir et al., 2010, Luo et al., 2011, Bari et al., 2012] observed clear grain size redistribution caused by fractures of sand grains during experiment. Thus, a successful numerical model of soils should take into account fracture of sand grains in order to accurately predict the mechanical behavior of soils at high strain rate.

The Discrete Element Method (DEM) [Cundall and Strack, 1979] is often used in geotechnical engineering to simulate the motion of individual particles/grains within a deforming/flowing granular medium[Horner et al., 2001, Hopkins, 2004, Zhu et al., 2008, Yan et al., 2010, O'Sullivan, 2011, Knuth et al., 2012]. Many investigations have constructed particle fracture models in DEM and have used these models to study mechanical behavior of soils and to simulate experiments. A common research approach is to model particle fracture using spring or beam elements to bond many small sub-particles (e.g. spheres, cylinders and triangles), forming a large single particle; breakage of these bonds will allows subdivision of the large particle[Potapov and Campbell, 1994, Cheng et al., 2003, Robertson and Bolton, 2001, Hosseininia and Mirghasemi, 2006, Refahi et al., 2010, Cil and Alshibli, 2012, André et al., 2013]. This method has been used in studies of single-particle fracture or small-scale problems. However, it is too expensive to be applied in large simulations. Åström and Herrmann [1998], Tsoungui et al. [1999], Ben-Nun et al. [2010], Ben-Nun and Einav [2010], McDowell and de Bono [2013] constructed a spherical DEM model in which spherical particles are allowed to break into several smaller spheres based on some stress-based fracture criterion. Their method was applied successfully to phenomena such as self-organization, particle size redistribution, change of void ratio, and critical state by simulating compaction of soils with capability of particle fracture. Cundall and Hart [1985] proposed a 2-dimensional method to break polygons into two sub-polygons through the line connecting the two loading points with the maximum loads. In this model polygons can be broken in an arbitrary direction, which is determined by the loadings. This is shown to be a useful model in studying fracture initiation in rocks.

Although many researches have modeled particle fracture DEM, to the authors' knowledge, there is no research published to study numerically the mechanical behavior of soils under high strain-rate compressive loading, such as SHPB experiments. The motivation of this research is to develop a DEM model that is able to simulate SHPB experiments

at high strain-rate. At present, spheres have the fastest contact search algorithm in DEM [Cundall and Strack, 1979, Peters et al., 2009, Wellmann et al., 2008], followed by ellipsoids [Hopkins, 2004, Yan et al., 2010], poly-ellipsoids [Peters et al., 2009, Knuth et al., 2012], super-ellipsoids [Wellmann et al., 2008], super-quadrics [Wellmann and Wriggers, 2012] and polyhedra [Nezami et al., 2004, Hopkins, 2010]. Alternatively, a level set can be used to represent particle shapes such as in [Andrade et al., 2012], but the trade-off is a more costly contact detection algorithm and more memory requirements for the storage of the particles. In this research, we employ a balanced approach by using poly-ellipsoids, which approximate the geometry of complex particle shapes while providing the advantage of efficient ellipsoidal contact search algorithms. A general poly-ellipsoid is a compound, smooth, non-symmetric shape with each octant composed of an eighth of an ellipsoid [Peters et al., 2009]. Compared to spheres and ellipsoids, poly-ellipsoids are potentially non-symmetric, and thus have more resistance to rolling, which can lead to more physically-realistic results [Peters et al., 2009]. Also, as a poly-ellipsoid, the particle can be sub-divided into several different sub-poly-ellipsoids, upon which we can establish a efficient, first-order particle fracture model.

In our particle fracture model, the continuum/average stress within a particle and and the maximum tensile stresses in contacts will both be used as fracture criterion. It is experimentally observed (c.f. [Hardin, 1985, Lade et al., 1996]) that material strengths decreases for larger grains, due to the increased probability of defects exisiting within larger grains. This apparent size-dependence of material strength can be described by Weibull statistics theory [Tsoungui et al., 1999, Ben-Nun et al., 2010, Ben-Nun and Einav, 2010, McDowell and de Bono, 2013, Brzesowsky et al., 2011, Strack et al., 2015, Weibull, 1951], which is also included in our model.

2 Geometry of poly-ellipsoid

The poly-ellipsoid geometry is described following the definition by Peters et al. [2009]. As in Figure 1, eight different ellipsoids are combined together with smoothed surfaces to construct a poly-ellipsoid. Each octant of the poly-ellipsoid is composed of one eighth of an ellipsoid with its center at (x_0, y_0, z_0), whose implicit equation is

$$\left(\frac{x-x_0}{a}\right)^2+\left(\frac{y-y_0}{b}\right)^2+\left(\frac{z-z_0}{c}\right)^2=1 \tag{1}$$

where a, b and c are the three semi-principal-lengths of ellipsoid.

Suppose a_i, b_i and c_i are the semi-principal-lengths of the i^{th} ellipsoid in octant i ($i = 1, 2, \ldots, 8$). Then we can obtain six independent parameters based upon the smooth-condition of a poly-ellipsoid. For example, if ellipsoid 1 and ellipsoid 4 share the same boundary at plane $y = 0$, then the surface should be smooth along this boundary plane, which yields the condition $c_1 = c_4$. Similarly, relations between the eight sets of semi-

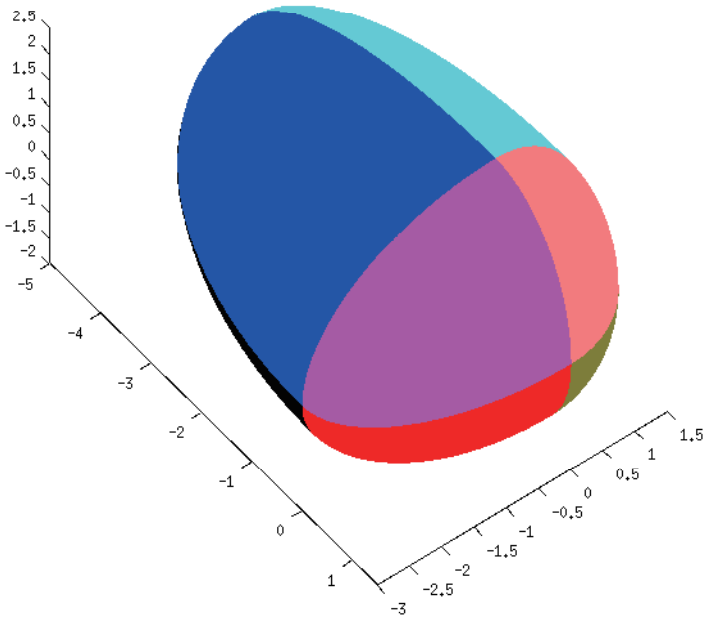

Figure 1: Poly-ellipsoid constructed from octants of eight ellipsoids, motivated by Peters et al. [2009].

principal-lengths can be described as [Peters et al., 2009],

$$\begin{aligned} a_2 = a_3 &= a_6 = a_7 &&= a^+ \\ a_1 = a_4 &= a_5 = a_8 &&= a^- \\ b_1 = b_2 &= b_5 = b_6 &&= b^+ \\ b_3 = b_4 &= b_7 = b_8 &&= b^- \\ c_1 = c_2 &= c_3 = c_4 &&= c^+ \\ c_5 = c_6 &= c_7 = c_8 &&= c^- \end{aligned} \tag{2}$$

where a^+, a^-, b^+, b^-, c^+ and c^- are the semi-principal-lengths of a poly-ellipsoid along positive and negative directions of the principal axes. Now we can see that the size and shape of poly-ellipsoids are controlled by these six independent parameters instead of only three parameters for ellipsoids. As a result, "sharper" and more realistic particle shapes can be represented with the six-parameter poly-ellipsoids versus the three-parameter ellipsoids.

3 Description of our particle fracture model in DEM

As shown in Figure 2, our adaptive particle fracture model has two steps: (1) Flag a particle that may break, and sub-divide it into sub-poly-ellipsoids bonded by springs as in Figure 3. At this time, the sub-particles will have the same kinetic state, such as velocity and angular velocity as the original particle. (2) Each spring has a breakage criterion, and when

all springs for a sub-poly-ellipsoid have broken, this sub-particle is free and it can be sub-divided and broken again. With the help of springs that are bonding sub-particles, this adaptive particle fracture model can represent the three different fracture modes, namely the opening mode, shearing mode and tearing mode.

In this brief introduction we identify several important aspects of the particle-fracture model that govern when and how a particle is sub-divided. The "when" depends on the breakage criterion and material strength of sand grains; the "how" depends on the determination of the break plane and the configuration of springs.

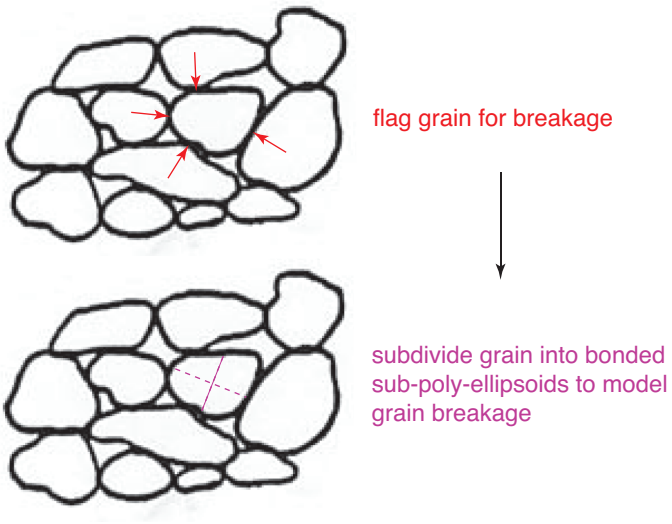

Figure 2: The adaptive fracture model has two steps, (1) sub-divide a particle into several sub-particles bonded by springs, and (2) break the springs.

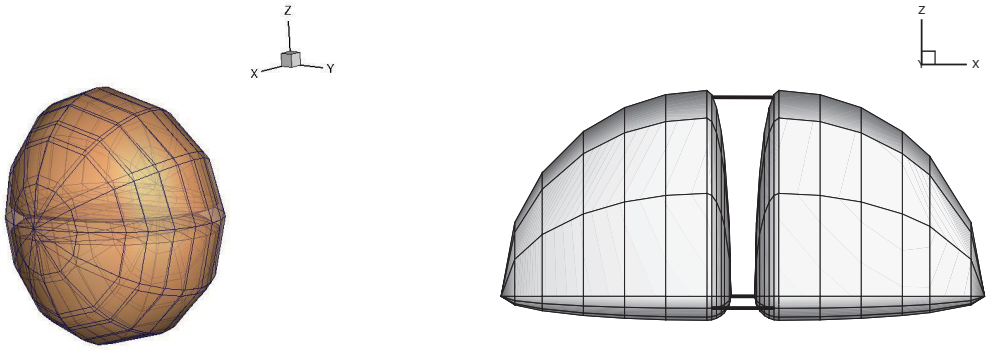

(a) (b)

Figure 3: A poly-ellipsoid is sub-divided into sub-poly-ellipsoids bonded by springs.

3.1 Models and parameterization describing DEM particle fracture

Figure 4 and 5 show the tensile stress contours within disks under uniaxial compression and biaxial compression, respectively, simulated using a Material Point Method (MPM) code, Uintah [Guilkey et al., 2009]. The stress scale is in units of Pa and the scale is in [m]. The scale of the problem is more appropriate for the contact and fracture of boulder sized spheres, but the observation of a tensile region outside the contact area and the effect of loading condition are equally valid for small or large sized grains. Figure 4 shows that there is region of tensile stress inside the disk under uniaxial compression, which is along the loading axis. Aside from the stress concentration near the contact point, the maximum principal stress is at the center of the disk. However, the interior tensile stresses are not obvious and are much smaller within the disk under biaxial compression (Figure 5). Because of this, particles under uniaxial compression fail at a lower force than those under biaxial compression. This demonstrates that the mode of loading, not simply the magnitude of the forces, bust be accounted for when estimating a failure stress for a particle.

The fracture criterion for a particle should reflect this dependence on loading mode, i.e. particles under uniaxial compression should fail more easily than particles under biaxial compression/triaxial compression in 3D. The ideal approach would be to find a closed-form solution for tensile stress σ_t in the center of the ellipsoid/sphere, and then allow the particle to break if $\sigma_t > \sigma_c$, where σ_c is the tensile strength for the particle. However, a tractable closed-form elasticity solution does not exist for general loading of a poly-ellipsoid. To approximate the peak stress, we use a continuum/average stress for single particle and input this continuum/average stress into the Hoek-Brown fracture criterion [Hoek and Martin, 2014] to determine whether particles will fail under a given loading. The Hoek-Brown fracture criterion is selected because the abundance of experimental data that is suitable for calibration of the model parameters [Hoek and Martin, 2014], as well as the previously demonstrated capability of the model to predict brittle failure in numerical simulations [Lan et al., 2010]. Other researchers have used a Brazilian (*c.f.,* Tsoungui et al. [1999], Ben-Nun et al. [2010], Ben-Nun and Einav [2010]) or octahedral shear stress (*c.f.,* McDowell and de Bono [2013]) criterion for their DEM particle fracture model; justifying the use of such models with the assertion that particles under symmetric loading will not break. However, our numerical and experimental evidence shows that particles under such loadings may, in fact, be fractured.

3.1.1 Continuum/average stress formulation for a single DEM particle

Before the discussion of Hoek-Brown fracture criterion, let us first look into the continuum/average stress for a single particle. Andrade et al. [2012] derived a formulation for the continuum/average stress of an individual particle in a static state. We extend this analysis to compute the continuum/average stress for an individual particle in a dynamic state as follows.

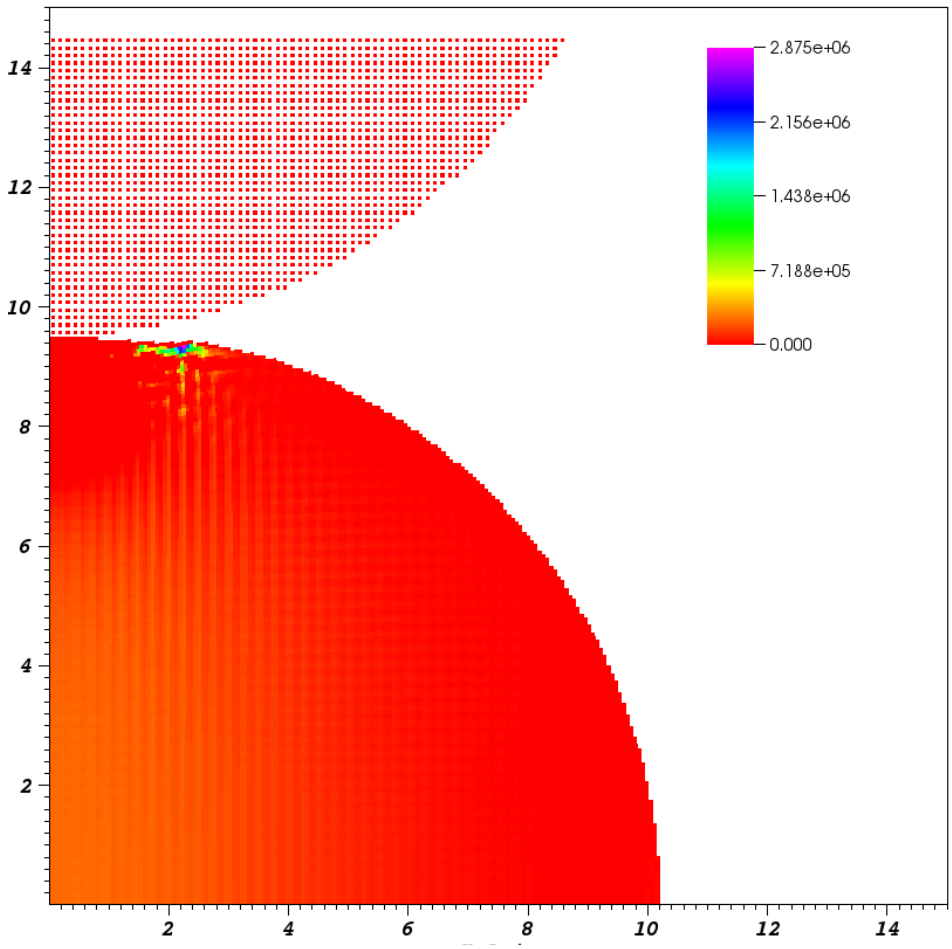

Figure 4: Contour of tensile stress inside a disk under uniaxial compression, simulated using Uintah. Aside from the stress concentration near the contact point, the largest tensile stresses occur at the center of the disk.

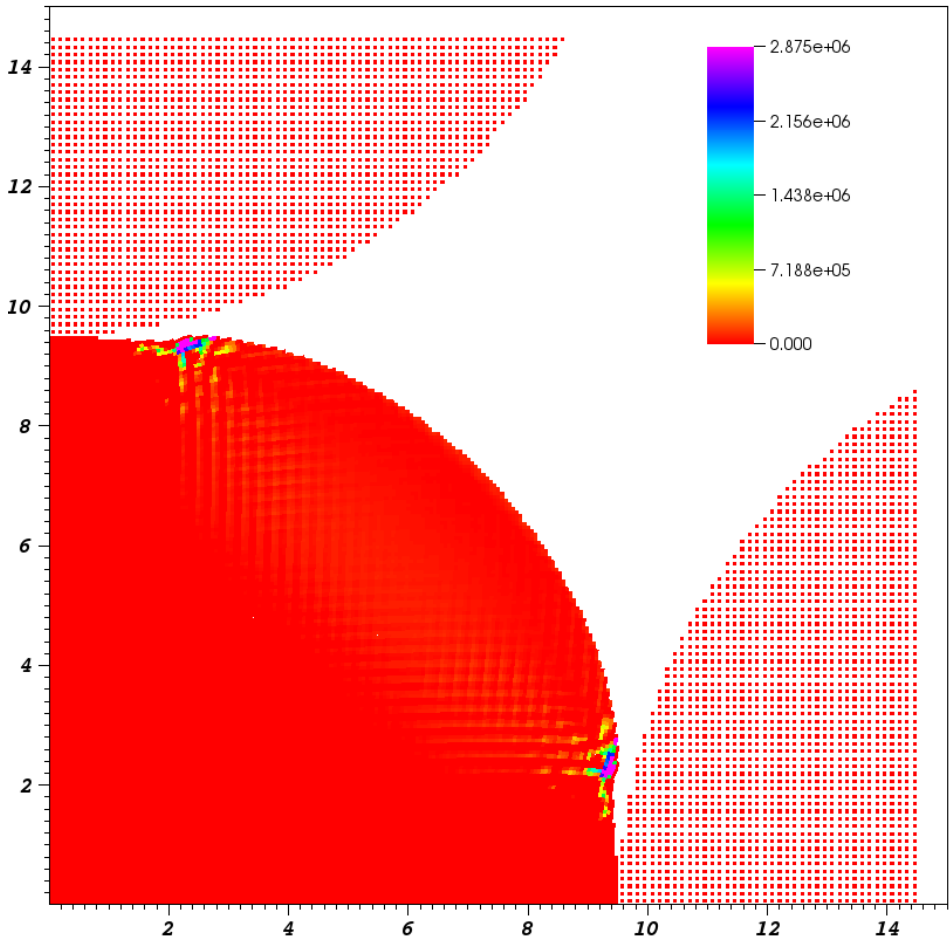

Figure 5: Contour of tensile stress inside a disk under biaxial compression, simulated using Uintah. The internal tensile stresses are lower than for the uniaxial loading case.

From the Gaussian theorem, we have

$$\begin{aligned}\frac{\partial \sigma_{ij} x_k}{\partial x_j} &= \frac{\partial \sigma_{ij}}{\partial x_j} x_k + \sigma_{ij} \frac{\partial x_k}{\partial x_j} \\ &= \frac{\partial \sigma_{ij}}{\partial x_j} x_k + \sigma_{ij} \delta_{kj} \\ &= \frac{\partial \sigma_{ij}}{\partial x_j} x_k + \sigma_{ik}.\end{aligned} \tag{3}$$

Thus we have

$$\sigma_{ik} = \frac{\partial \sigma_{ij} x_k}{\partial x_j} - \frac{\partial \sigma_{ij}}{\partial x_j} x_k. \tag{4}$$

Since $\frac{\partial \sigma_{ij}}{\partial x_j} + \rho g_i = \rho a_i$, we know

$$\sigma_{ik} = \frac{\partial \sigma_{ij} x_k}{\partial x_j} - \rho \left(a_i - g_i\right) x_k. \tag{5}$$

Then the average stress for individual particle is

$$\overline{\sigma_{ik}^p} := \frac{1}{\Omega_p} \int_{\Omega_p} \sigma_{ik} \, d\Omega_p \tag{6}$$

$$= \frac{1}{\Omega_p} \int_{\Omega_p} \frac{\partial \sigma_{ij} x_k}{\partial x_j} \, dv - \frac{1}{\Omega_p} \int_{\Omega^p} \rho \left(a_i - g_i\right) x_k \, dv \tag{7}$$

$$= \frac{1}{\Omega_p} \sum_{\alpha=1}^{N_c^p} \left(f_i^\alpha x_k^\alpha\right) - \frac{\rho^p}{\Omega_p} \int_{\Omega_p} a_i x_k \, dv + \frac{\rho^p}{\Omega_p} g_i \int_{\Omega_p} x_k \, dv, \tag{8}$$

where Ω_p is the particle domain, $\mathbf{g}$ gravity and $\mathbf{a}$ acceleration. Notice that from Eq.(7) to (8), we use

$$\begin{aligned}\int_{\Omega_p} \frac{\partial \sigma_{ij} x_k}{\partial x_j} \, dv &= \int_{\Gamma^p} \sigma_{ij} x_k n_j \, da \\ &= \sum_{\alpha}^{N_c^p} f_i^\alpha x_k^\alpha.\end{aligned} \tag{9}$$

Acceleration $\mathbf{a}$ for point $\mathbf{x}$ can be calculated as

$$\begin{aligned}\mathbf{a} &= \mathbf{a}_o + \boldsymbol{\alpha} \times \mathbf{d} + \boldsymbol{\omega} \times (\boldsymbol{\omega} \times \mathbf{d}) \\ &= \mathbf{a}_o + \boldsymbol{\alpha} \times (\mathbf{x} - \mathbf{x}_o) + \boldsymbol{\omega} \times [\boldsymbol{\omega} \times (\mathbf{x} - \mathbf{x}_o)]\end{aligned} \tag{10}$$

We can calculate $\int_{\Omega_p} \rho \mathbf{a} \otimes \mathbf{x} \, d\Omega_p$ in Eq.(8) in a local coordinate system whose origin is fixed at the center-of-geometry of the poly-ellipsoid and then transfer the local matrix to get

$\int_{\Omega_p} \rho \mathbf{a} \otimes \mathbf{x}\, d\Omega_p$ in the global system.

$$\int_{\Omega_p} \rho \mathbf{a} \otimes \mathbf{x}\, d\Omega_p = \rho \int_{\Omega_p} a_i x_j \, d\Omega_p \tag{11}$$

$$= \rho \int_{\Omega_p} \left[a_i^o + \epsilon_{lki} \alpha_l x_k + \epsilon_{lki} \omega_l \epsilon_{mnk} \omega_m x_n \right] x_j \, d\Omega_p \tag{12}$$

$$= \rho \left[a_i^o \int_{\Omega_p} x_j \, d\Omega_p + \epsilon_{lki} \alpha_l \int_{\Omega_p} x_k x_j \, d\Omega_p + \epsilon_{ilk} \epsilon_{mnk} \omega_l \omega_m \int_{\Omega_p} x_n x_j \, d\Omega_p \right] \tag{13}$$

3.1.2 Hoek-Brown fracture criterion

The Hoek-Brown fracture criterion is stated as [Hoek and Martin, 2014]

$$\sigma_1 = \sigma_3 + \sigma_c \sqrt{m_i \frac{\sigma_3}{\sigma_c} + 1}, \tag{14}$$

where m_i is a material constant, σ_c is the compressive strength of the particle, and σ_1 and σ_3 are the major and minor principle stress, respectively, where we use the convention that positive stresses denote compression. Figure 6 is a plot for Hoek-Brown criterion with $m_i = 20.56$ and $\sigma_c = 592\, MPa$.

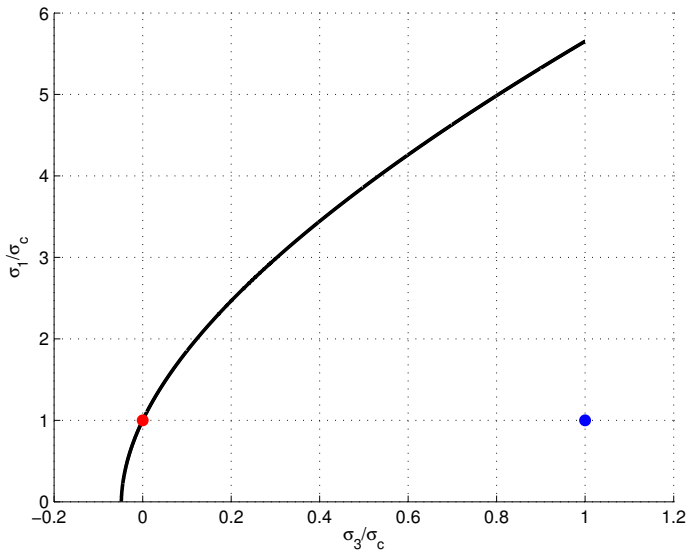

Figure 6: Plot for Hoek-Brown fracture criterion with $m_i = 20.56$ and $\sigma_c = 592\, MPa$. The red and blue dots indicate the stresses for a critical uniaxial-compression stress state and a corresponding sub-critical biaxial stress state.

We now evaluate whether the Hoek-Brown fracture criterion based on a continuum/average stress formulation is consistent with the observations in Figure 4 and 5, namely that particles under uniaxial compression are easier to break than those under biaxial compression. We explore this question with a 2D example as follows.

First, let us calculate the continuum/average stress for particles under uniaxial and biaxial compression. For particle under uniaxial compression as in Figure 7, the continuum stress is

$$\boldsymbol{\sigma} = \frac{1}{\pi r^2}\begin{bmatrix} 0 & 0 \\ 0 & 2rF \end{bmatrix}. \tag{15}$$

Here the sign convention in the Hoek-Brown fracture criterion is used, namely that positive stresses are compressive. With the Hoek-Brown sign convention, for this uniaxial compression loading, $\sigma_1 = \frac{2rF}{\pi r^2} = \frac{2F}{\pi r}$ and $\sigma_3 = 0$. This continuum stress measure describes an average over the particle domain, and cannot therefore reflect the possibility of tensile failure at points within a particle, as there is no tensile stress in this result.

Particles under uniaxial compression loadings can be fractured in the Hoek-Brown criterion, for example when $\sigma_3 = 0$ and $\sigma_1 > \sigma_c$. This capability is necessary for a suitable fracture criterion, since experience and many experiments [Gallagher et al., 1974, Gallagher Jr et al., 1976, Salman and Gorham, 2000, Nakata et al., 2001, Brzesowsky et al., 2011] conclusively demonstrate that sand grains can break under uniaxial compression loadings.

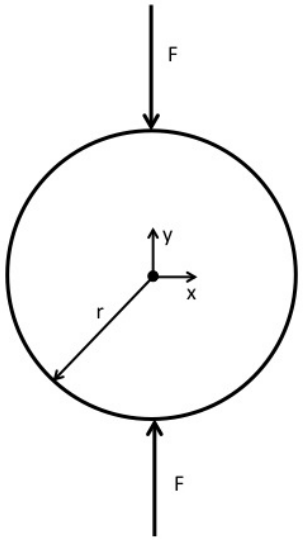

Figure 7: Illustration of particle under uniaxial loading in 1D.

For particle under biaxial compression as in Figure 8, the continuum stress is

$$\boldsymbol{\sigma} = \frac{1}{\pi r^2}\begin{bmatrix} 2rF & 0 \\ 0 & 2rF \end{bmatrix}. \tag{16}$$

Then for this biaxial compression loading, $\sigma_1 = \sigma_3 = \frac{2rF}{\pi r^2} = \frac{2F}{\pi r}$.

The red dot in Figure 6 shows a stress state corresponding to particle failure under uniaxial compression, with $\sigma_1 = \sigma_c$ and $\sigma_3 = 0$. The blue dot in this figure shows a case of biaxial loading with the same magnitude force for which the state is well within the fialure surface. Thus, it shows that with this model particles under biaxial compression are more difficult to break than particles under uniaxial compression, consistent with experimental and numerical evidence.

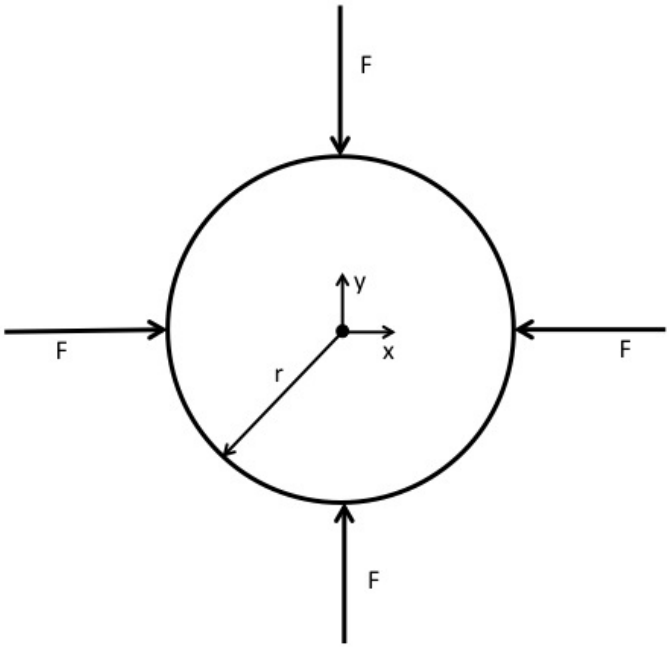

Figure 8: Illustration of particle under biaxial loading in 2D.

3.1.3 Local tensile stress fracture criterion

Particles under equibiaxial compression can never break in Hoek-Brown fracture criterion as shown in Figure 6. However, we can imagine that physically there must exist some load that will induce particle failure under biaxial compression loading. In consideration of this physical reality, we introduce an additional fracture criterion determined by the maximum tensile stress in contact areas on a particle. This means that we will check each particle in simulations by two fracture criteria, either of which, when satisfied, will cause fracture of the particle. Ben-Nun and Einav [2010] have also considered the possibility of contact stress failure, but we use an entirely different approach that introduces a strong mechanics foundation.

We compute the contact force at each contact point based on the overlap between two ellipsoids using Hertzian contact theory, and then calculate the maximum tensile stress in this contact area following the method described in [S.P. Timoshenko, 1970]. Suppose contact radius a of a contact between two particles has already been calculated from Hertz-Mindlin contact theory [Mindlin, 1949], and R_1 and R_2 are curvatures at the contact points of the two particles, the maximum tensile stress at this contact area is [S.P. Timoshenko, 1970]

$$\sigma_t = \frac{1-2\mu}{3} q_0, \tag{17}$$

where $q_0 = \frac{3F}{2\pi a^2}$ is the maximum pressure in contact area, and F is contact force which is already calculated from Hertz-Mindlin contact theory. According to S.P. Timoshenko [1970], the normal stress becomes zero along the circular boundary of the contact area, at which point there exists a state of pure shear, which is $0.133q_0$ for sands with Poisson's

ratio $\nu = 0.3$. This means that stress along the boundary of the contact area is already very small, and the extent of influence of the contact stress is highly localized. Suppose we have two spherical sand grains in contact with force $F = 10\,N$, where both grains have Young's modulus 60 GPa and Poisson's ratio $\nu = 0.25$, then the contact radius is $a = 1.1356\sqrt[3]{\frac{F}{E}\frac{R_1R_2}{R_1+R_2}} = 6.2494 \times 10^{-4}\sqrt[3]{\frac{R_1R_2}{R_1+R_2} \cdot 1\,\mathrm{m}^2}$. If we further assume $R_1 = R_2 = 0.3\,\mathrm{mm}$, then the contact area is approximately equal to $3.0628 \times 10^{-3}A$, where A is the surface area of the sphere. This example demonstrates that the contact area is extremely small compared to the surface area of the particle. Because of this, for nearly spherical bodies of comparable size, the contact points never be close enough for there to be significant interactions between the contact stresses. Thus, even if there are multiple contact points on a particle, the local maximum tensile stress for each contact can be computed from Equation (17) with no needs to consider influence from other contacts.

We then identify a critical contact at any point where maximum tensile contact stress exceeds the tensile strength of the particle. If three or more critical points exist, the contact fracture criterion for the particle is met, and the particle will break. The limitation of this fracture criterion is that it does not distinguish between different loading states (for example, biaxial or triaxial), and the particle failure depends only on the maximum tensile stress in each contact. However, by combining the contact failure criterion with the Hoek-Brown continuum/average stress fracture criterion, we are able to overcome the limitations of using either method individually and better describe particle failure in diverse modes of loading.

3.2 Defining strength for the "break" criteria

To apply the fracture criteria and determine whether a particle will break at a given load it is necessary to define and parameterize an appropriate material strength measure for each criterion. In our work we have two material strengths to be determined in our fracture model, a compressive strength for the Hoek-Brown criterion and a local tensile strength for contact failure. Initially, we would like parameterize the failure strength in these models with experimental data for single sand-grain fracture. We complete this parameterization process for one such experiment[1], for which the comparison between simulation and experiment are given in Section 4. From this comparison, we can see that our model is able to fit the experimental curve very well. However, we found that there was significant test-to-test variability in the available experimental results for single particle fracture.

To extend our analysis we apply our analysis to the published results from investigations by [Hoek and Martin, 2014, Brzesowsky et al., 2011]. Brzesowsky et al. [2011] did many experiments (200 sand grains for each size) for single sand grain fracture under diametric compression between flat platens. They calculated tensile strengths in contacts for each fractured sand grain using Hertzian contact theory, and generated a relation of tensile strength and grain size. These data were a valuable resource for parameterizing the tensile strength for the contact-stress particle fracture model. Based on the results of [Hoek and Martin, 2014, Brzesowsky et al., 2011], we also introduce a Weibull-distributed variable strength as

[1]The results are one example from numerous tests from unpublished results from Prof. Khalid Alshibli's group at University of Tennessee Knoxville

done in Ben-Nun et al. [2010],

$$\sigma_f(P) = \sigma_{fM} \ln(1/P)^{1/w} (x/x_M)^{-2w} \tag{18}$$

where σ_{fM} is the reference strength for a particle with reference size x_M (here we use the equivalent radius calculated as $r = (3V/4\pi)^{1/3}$), $P \in (0,1)$ is a uniformly distributed variable, and w is Weibull's modulus.

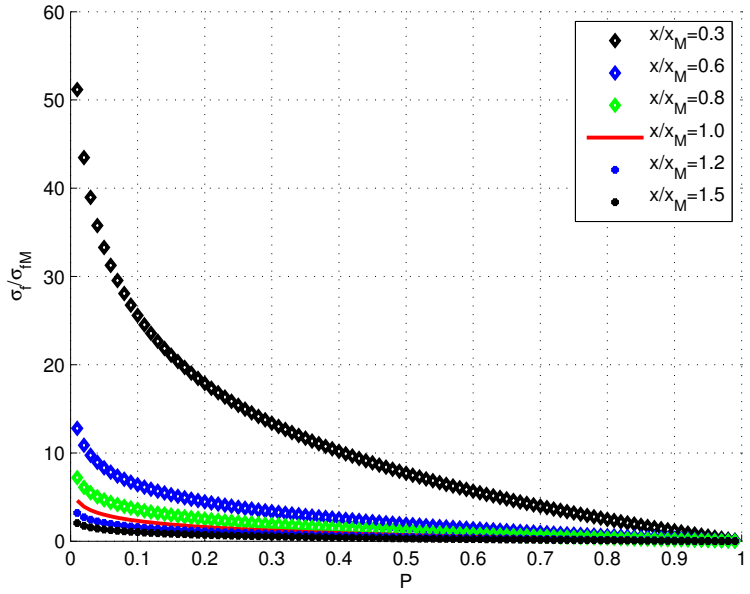

Figure 9: The Weibull function as $w = 1$, this function can reflect size effects of sand grains and also Weibull's statistics of strength [Ben-Nun et al., 2010]. Smaller particles are much stronger than larger particles. For equally sized particles, such as $x/x_M = 1.0$, the uniformly distributed variable P introduces variation to the particles' strengths.

This Weibull function is used to assign different strength values to particles even if their shapes are exactly the same as shown in Figure 9, which we believe is necessary since it is very possible that the initial flaw distribution will vary from particle to particle. Similarly, our compressive strength σ_c and material constant m_i in the Hoek-Brown fracture criterion are from Hoek and Martin [2014].

3.3 Determination of the fracture plane location and orientation

Once a particle fracture criterion has been met, we next determine the plane along which the particles will break. We call this plane the *break plane*. This determination is important since the break plane will affect how well the generated sub-particles can capture the original particle's shape. Åström and Herrmann [1998], Tsoungui et al. [1999], Ben-Nun et al. [2010], Ben-Nun and Einav [2010], McDowell and de Bono [2013] used spheres or circles to represent their particles in DEM, and their fractured spheres/ circles are replaced by a set of smaller spheres/circles. In some of these works, to account for the reduction in total volume of the

smaller particles relative to that of the original particle, the authors either increase density of the smaller particles, expand the particles' volume over a short time, or entirely neglect the mass loss. However, none theses choices can avoid some contact loss between the sub-particles and the contacting neighbors of the original particle. In our method there is a small loss of contact in sub-division, but the contact loss in our method is less severe than in [Åström and Herrmann, 1998, Tsoungui et al., 1999, Ben-Nun et al., 2010, Ben-Nun and Einav, 2010, McDowell and de Bono, 2013], and we have implemented a technique to reduce the loss of contact, as described in Section 3.3.1.

Gallagher Jr et al. [1976], Salman and Gorham [2000] observed in their experiments that a break plane is a meridian plane, so we assume that a break plane will pass through the centroid in our particle fracture model. We have two fracture criteria in our particle fracture model, for which we have very different methods to determine break plane. In the Hoek-Brown fracture criterion, particles are fractured based on their continuum/average stresses. The ideal break plane for this case would be normal to the minor principle direction of stress. However, there is a limitation in our particle fracture model that we have to break particles along principle directions of the poly-ellipsoid. This requirement allows us to sub-divide a poly-ellipsoid into several poly-ellipsoids that fit the original shape well enough to mitigate loss of contact. To select the break plane, we calculate the normal stress components along the three principle directions of the poly-ellipsoid, and select the plane at which there is the largest tensile normal stress.

In the fracture criterion by critical contacts, the break plane is defined by the 3 critical contacts. The need for three points to define the plane as well as qualitative observations of particle failure form the basis for our requiring 3 critical contacts for this mode of fracture. The ideal break plane has the orientation of a plane passing through the critical points, but has been shifted to pass through the centroid of the poly-ellipsoid as shown in Figure 10. However, considering the limitation of the determination of break plane, we have to break poly-ellipsoids along their principle directions in geometry. There are three candidate break planes, whose unit normal vectors in the local coordinate system of the poly-ellipsoid are $\mathbf{i} = (1, 0, 0)$, $\mathbf{j} = (0, 1, 0)$ and $\mathbf{k} = (0, 0, 1)$, respectively. We can denote the unit normal vector of the plane determined by the 3 critical contacts as $\mathbf{n}$. We then select as the break the candidate direction whose normal direction has the smallest cross angle with $\mathbf{n}$ by comparing the magnitude of the dot product $\mathbf{n} \cdot \mathbf{i}$, $\mathbf{n} \cdot \mathbf{j}$ and $\mathbf{n} \cdot \mathbf{k}$.

Our method introduces a nonphysical constraint by allowing fracture only along the principal planes of the poly-ellipsoid. While this imparts a significant gain in efficiency, validation of the method requires that we assess the extent to which this constraint affects the accuracy of the bulk response of a granular material. This assessment is difficult through direct experimental validation, as there are a great many factors that could affect the overall accuracy of the simulation method. To study the specific effect of the breakage planes, we study the response for the special case of spherical poly-ellipsoids. The principle directions of the spherical particles can be instantaneously rotated to an arbitrary direction so the break plane can produce the ideal orientation. Here, the rotation of break plane is a strictly geometric process, and it will not be included in calculation of angular velocity. The response of the system with freely orientated break planes can then be compared to the identical system with fixed principal directions (either uniformly or randomly oriented in each sphere). In this way the limitation of the break plane constraint can be observed directly.

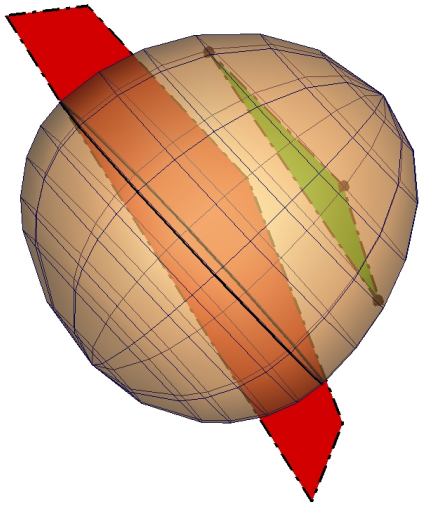

Figure 10: The ideal break plane should meet two requirements: (1) parallel to the plane generated the 3 critical contacts, (2) should pass through particle centroid. Suppose the black points are the critical contacts, and red plane is the ideal break plane, which is parallel to the green plane and passing through the particle centroid. Constrained by allowing fracture only along the principle planes, the actual break plane in the model is shown as the black curves.

In the following, we will describe a technique to reduce contact loss caused by sub-division, by rotating the break plane slightly, and thus rotating the resulting geometry of sub-poly-ellipsoids.

3.3.1 Random slight rotation of break plane

Compare the sub-poly-ellipsoids and the original poly-ellipsoid as in Figure 11, we can see that the generated sub-poly-ellipsoids cannot capture the original shape perfectly, thus we may lose some of the contacts that were on the original particle. To reduce the effect of loss of contacts, we can rotate slightly the break plane as shown in Figure 12. Further justification of the rotation of the break plane derives from the tensile stresses occuring outside the contact region, which may act as a source of fracture initiation as shown in Figs. 4 and 5.

The following key points should be emphasized (1) Only spheres permit free rotation of their break plane. (2) Currently, our sub-division is along the principle directions of spheres (we may rotate the principle directions to the ideal break plane for spheres). Then the slight rotation of break plane can be converted to slight rotation of principle directions. (3) To simplify implementation, we rotate the principle directions in the local coordinate system of the sphere first and then transfer the rotated principle directions to the global coordinate system. Suppose $\mathbf{a} = (1, 0, 0)$, $\mathbf{b} = (0, 1, 0)$ and $\mathbf{c} = (0, 0, 1)$ are the principle directions of a sphere in its local coordinate system, and α, β, γ are rotation angles along the three axes in the local coordinate system. α, β, γ are small random angles in $[-\theta, -0.5\theta] \cup [0.5\theta, \theta]$. Then

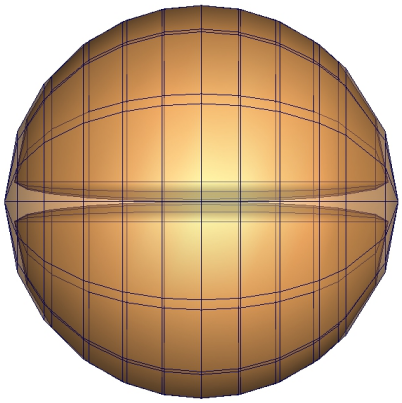

Figure 11: The generated sub-poly-ellipsoids cannot capture the shape of the original poly-ellipsoid perfectly, thus there will be loss of contacts during sub-division. The surface mesh shown is added to more clearly distinguish the surface of the original particle from that of the sub-particles, the actual geometry is a smooth polyellipsoid.

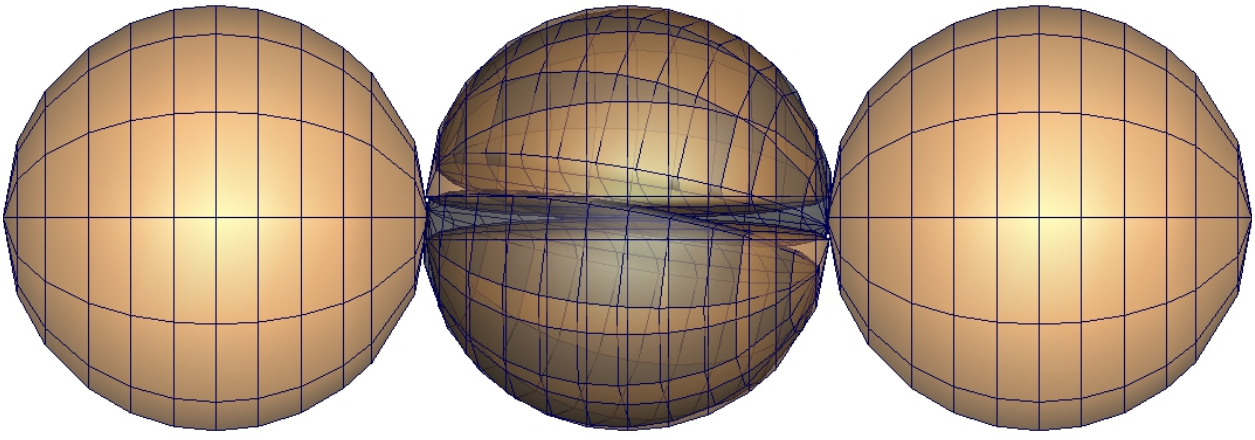

Figure 12: Slight rotation of break plane can reduce the loss of contacts. The orange sub-particles are without random rotation, while grey ones are after random rotation by angle of $0.1745\,rad\,(10.0^{\circ})$, which can better-recover the original contact.

rotation matrix is [MathWorld]

$$\mathbf{R}(\alpha,\beta,\gamma) = \mathbf{R}_x(\alpha)\,\mathbf{R}_y(\beta)\,\mathbf{R}_z(\gamma) \tag{19}$$

$$= \begin{bmatrix} 1 & 0 & 0 \\ 0 & \cos\alpha & \sin\alpha \\ 0 & -\sin\alpha & \cos\alpha \end{bmatrix} \begin{bmatrix} \cos\beta & 0 & -\sin\beta \\ 0 & 1 & 0 \\ \sin\beta & 0 & \cos\beta \end{bmatrix} \begin{bmatrix} \cos\gamma & \sin\gamma & 0 \\ -\sin\gamma & \cos\gamma & 0 \\ 0 & 0 & 1 \end{bmatrix}. \tag{20}$$

The rotated principle directions in the local coordinate system will then be

$$\mathbf{a}' = \begin{bmatrix} \cos\beta\,\cos\gamma \\ \cos\gamma\,\sin\alpha\,\sin\beta - \cos\alpha\,\sin\gamma \\ \sin\alpha\,\sin\gamma + \cos\alpha\,\cos\gamma\,\sin\beta \end{bmatrix} \tag{21}$$

$$\mathbf{b}' = \begin{bmatrix} \cos\beta\,\sin\gamma \\ \cos\alpha\,\cos\gamma + \sin\alpha\,\sin\beta\,\sin\gamma \\ \cos\alpha\,\sin\beta\,\sin\gamma - \cos\gamma\,\sin\alpha \end{bmatrix} \tag{22}$$

$$\mathbf{c}' = \begin{bmatrix} -\sin\beta \\ \cos\beta\,\sin\alpha \\ \cos\alpha\,\cos\beta \end{bmatrix}. \tag{23}$$

Transforming the rotated principle directions to the global coordinate system will give us the new principle directions of perturbed sphere having a slight and random rotation, for which the break plane is also rotated slightly.

To determine the maximum rotation angle, (θ), considering the shape of a newly generated sub-poly-ellipsoid from sub-division of a sphere (Figure 13), we can use θ as shown in Figure 13. The movement of the centroid creates the gap between the generated sub-poly-ellipsoids and the original shape. It can be shown that $\theta = \arctan\left(\frac{1}{5}\right) = 0.1974\,\text{rad}$ (or 11.3°).

3.3.2 Geometry of the sub-poly-ellipsoid

After the break plane is determined, we need to calculate the geometry of the newly formed sub-poly-ellipsoids. There are three pieces of geometric information for the sub-poly-ellipsoid that we need to know: (1) its principal directions, here we use the same principle directions as the original poly-ellipsoid in order to capture the original shape as much as possible; (2) its principal lengths; and (3) the coordinate of its centroid.

The projected ellipse of a sub-poly-ellipsoid in the $x'z'$ plane is taken as an example, as shown in Figure 14. In Figure 14, the centroid of the sub-poly-ellipsoid is shifted from centroid of the original poly-ellipsoid, O to O'. We assume $a'_+ = \frac{9}{10}a_+$ in our model. With this assumption, the centroid of the sub-poly-ellipsoid can be determined. Next, its principle lengths will be calculated as follows.

The equation of the projection of the sub-poly-ellipsoid in octant 1 is

$$\frac{(x' - \frac{1}{10}a_+)^2}{(r_a a_+)^2} + \frac{(z')^2}{(r_c c_+)^2} = 1 \tag{24}$$

where r_a and r_c is the length ratio of $(a_+)'$ and $(c_+)'$ to (a_+) and (c_+), respectively.

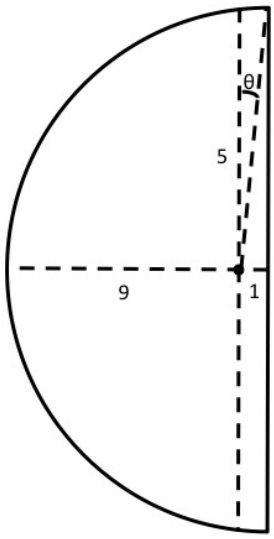

Figure 13: Schematic illustrating the method to determine the maximum rotation angle, θ by movement of the centroid. The geometric parameters 1, 9, and 5 relate to the geometry of the sub-poly-ellipsoid, described in Section 3.3.2.

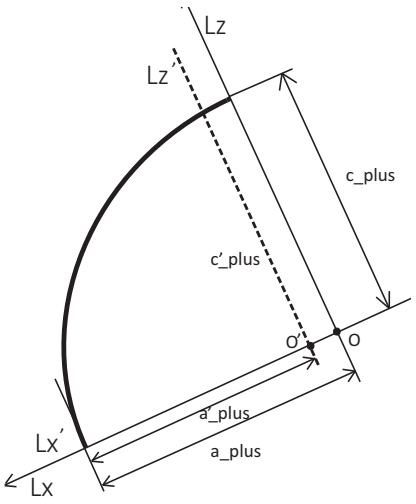

Figure 14: The principle lengths of sub-poly-ellipsoids.

Equation (24) can be written as

$$\begin{aligned} x' &= \frac{1}{10}a_+ + r_a a_+ \sin(\alpha) \\ z' &= r_c c_+ \cos(\alpha) \\ \alpha &\in [0, \frac{\pi}{2}]. \end{aligned} \tag{25}$$

The point (x', z') should be always inside of the original poly-ellipsoid for all α, which means

$$\frac{(\frac{1}{10}a_+ + r_a a_+ \sin\alpha)^2}{(a_+)^2} + \frac{(r_c c_+ \cos\alpha)^2}{(c_+)^2} \leq 1 \tag{26}$$

If we choose $r_a = 0.9$, then

$$r_c^2 \cos^2\alpha + 0.81 \sin^2\alpha + 0.18 \sin\alpha - 0.99 \leq 0 \tag{27}$$

which will lead to

$$r_c \leq \sqrt{\frac{0.99 - 0.81\sin^2\alpha - 0.18\sin\alpha}{\cos^2\alpha}}, \alpha \in [0, \frac{\pi}{2}] \tag{28}$$

From which, we can solve for the maximum $r_c = 0.9486833$.

3.3.3 Treatment of poorly shaped poly-ellipsoids

For poorly shaped poly-ellipsoids, i.e. those with small radii of curvature (*i.e., sharp*), we need to also introduce some geometry constraints on their sub-divisions to avoid unreasonably sharp sub-poly-ellipsoids features. Sharp poly-ellipsoids are undesirable, because they are nonphysical and may cause numerical problems.

Let us denote $a_{\min}$ as the smaller length between a^+ and a^- of a poly-ellipsoid, while $a_{\max}$ is the larger one, with the same notation for b and c. The following are several cases of poly-ellipsoids.

Case (1), $a_{\min} > 0.2a_{\max}$, $b_{\min} > 0.2b_{\max}$, $c_{\min} > 0.2c_{\max}$ as in Figure 15. This kind of poly-ellipsoids is *normal*, not sharp, and their break planes are determined by the method described in Section 3.3. The majority of initial particles in our simulations are of this type.

Case (2), $a_{\min} < 0.2a_{\max}$, $b_{\min} < 0.2b_{\max}$, $c_{\min} < 0.2c_{\max}$ as in Figure 16; the three principle axes of the poly-ellipsoid have a bad length ratio, and we do not break this kind of particle.

Case (3), Two principle axes of the poly-ellipsoid have a bad length ratio, for example $a_{\min} < 0.2a_{\max}$, $b_{\min} < 0.2b_{\max}$, $c_{\min} > 0.2c_{\max}$, with $c^+ + c^- > 1.2\max(a_{\max}, b_{\max})$ as in Figure 17. In this case, the particle is broken along the plane constructed from the two principle axes with the bad length ratio, which is the xy plane in this example.

Case (4), two principle axes of the poly-ellipsoid have a bad length ratio, for example $a_{\min} < 0.2a_{\max}$, $b_{\min} < 0.2b_{\max}$, $c_{\min} > 0.2c_{\max}$, but with $c^+ + c^- < 1.2max(a_{\max}, b_{\max})$ as in

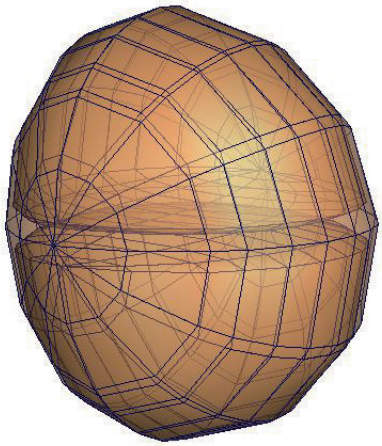

Figure 15: Division of a poly-ellipsoid of case (1) along the plane determined by particle average stress.

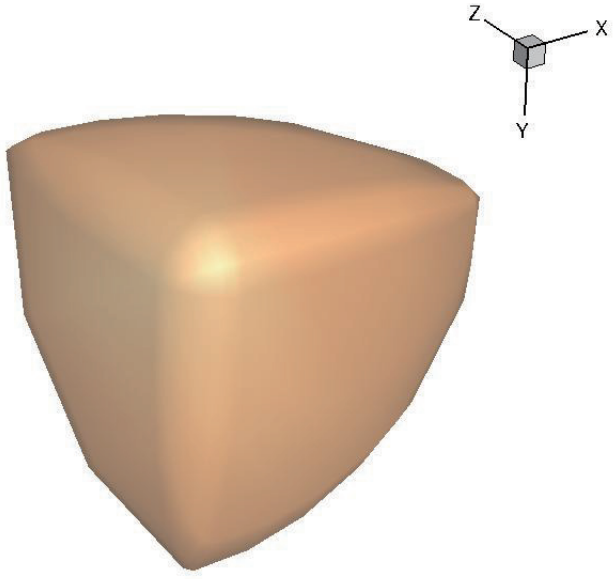

Figure 16: Do not break poly-ellipsoid with three bad ratio principle axles in case (2).

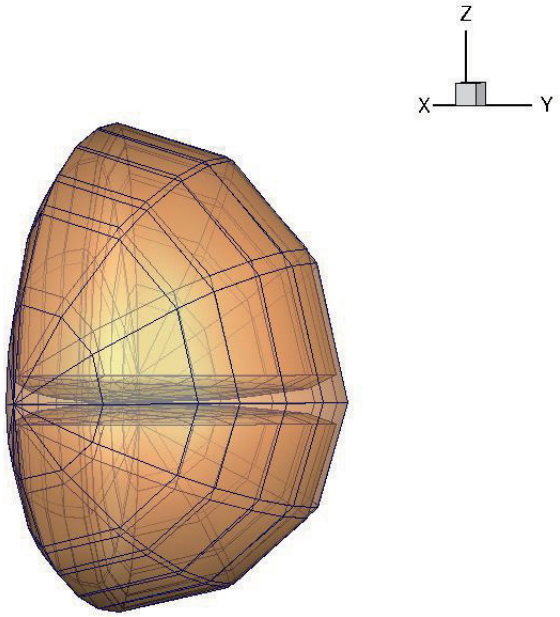

Figure 17: Divide the poly-ellipsoid case (3) along by the plane with two bad ratio principle axles.

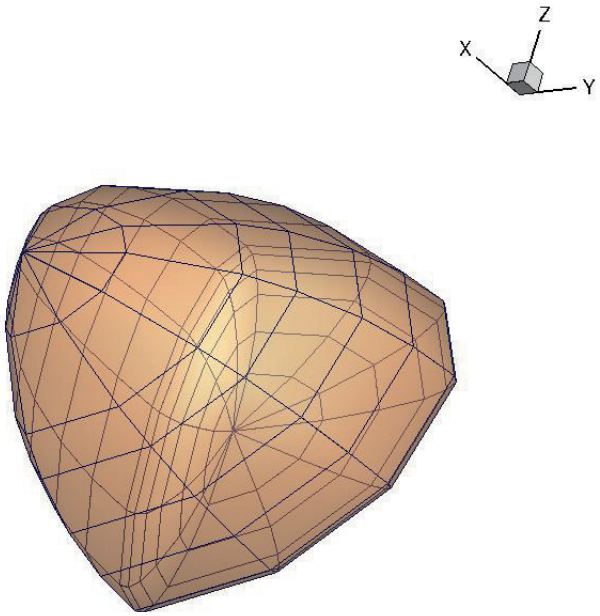

Figure 18: Do not break poly-ellipsoid of case (4).

Figure 18. In this case, as with Case 1, we do not break the particle.

Case (5), one principle axis of the poly-ellipsoid has a bad length ratio, for example $a_{\min} < 0.2a_{\max}$, $b_{\min} > 0.2b_{\max}$, $c_{\min} > 0.2c_{\max}$, as in Figure 19. In this case we follow the steps outlined in Algorithm 1.

Algorithm 1 Case 5 algorithm

```
if b+ + b− > 1.2(c+ + c−) then
    break along xz plane
else if c+ + c− > 1.2(b+ + b−) then
    break along xy plane
else
    if Using the Hoek-Brown criterion then
        calculate the principle stress along y and z axes
        if σ_y > σ_z then
            break along xz plane
        end if
    else                          ▷ Using contact maximum principal stress criterion
        Evaluate cross angles to candidate y and z directions
        Select break plane.
    end if
end if
```

Note that because of the geometric constraint, we can break a *normal*-shaped particle at most only three times, since after three sub-divisions, the generated sub-poly-ellipsoids will generally be poorly shaped, for which we do not allow further subdivision.

3.3.4 Shape transition of poorly shaped poly-ellipsoids

As a result of our geometric constraints, we can break a *normal*-shaped particle at most only three times, since after three sub-divisions, the generated sub-poly-ellipsoids will be very badly shaped, for which we prohibit sub-division in our particle fracture model. To relax this constraint and allow further subdivision, we may consider allowing these badly shaped poly-ellipsoids to slowly evolve to normal shape. This process is called *shape transition*. Shape transition should be very slow in order to avoid introducing large energy errors or sudden contacts caused in this process.

In our current implementation, we apply shape transition only to those sub-poly-ellipsoids generated from sub-divisions. Simply stated, the shape transition entails slowly moving the centroid of the bad particles in the direction with bad semi-lengths ratio, causing the geometry to evolve into a *normal* shape.

Suppose we have a particle with bad semi-length ratio in principle direction a, then the target poly-ellipsoid should have larger semi-lengths ratios as in Figure 20, such as

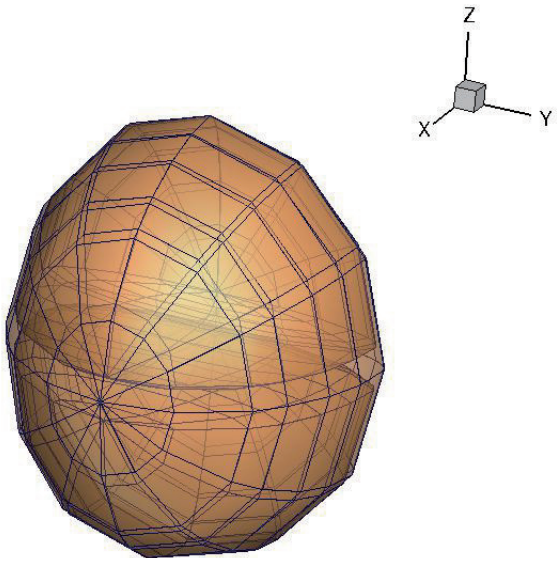

Figure 19: Division for a poly-ellipsoid of case (5), with break plane aligned along the xy plane.

$\frac{a'_{\min}}{a'_{\max}} > 0.25$. We have the relation

$$a'_{\min} = 0.25 a'_{\max} \tag{29}$$

$$a_{\min} + a_{\max} = a'_{\min} + a'_{\max} \tag{30}$$

Where $a_{\min}$, $a_{\max}$ are the current minimum and maximum semi-length in principle direction a, respectively. And $a'_{\min}$, $a'_{\max}$ are target semi-lengths. Then, the length that the centroid O should be moved is

$$\Delta O = a_{\max} - a'_{\max} \tag{31}$$

$$= a_{\max} - 0.8(a_{\min} + a_{\max}) \tag{32}$$

$$= 0.2a_{\max} - 0.8a_{\min}. \tag{33}$$

Suppose the shape transition will take n steps, then the centroid displacement in each step is $\Delta a = (0.2a_{\max} - 0.8a_{\min})/n$, $\Delta b = 0$, $\Delta c = 0$. Note that we do not introduce additional velocity from the movement of the centroid, but the shape transition may introduce a small error in the particle's mass and momentum.

For poly-ellipsoids with more than 1 bad-ratio axis, this process is applied to each principal direction sequentially in each step.

In applying the shape transition process, it was found that even when using 100 step divisions in the shape transition, very large and sudden contact forces will arise, which cause the particles to expand catastrophically. Other simulation results suggest that even when the transition response is stable, it may be unnecessary, so for subsequent results we turn off this shape transition feature in our particle fracture model.

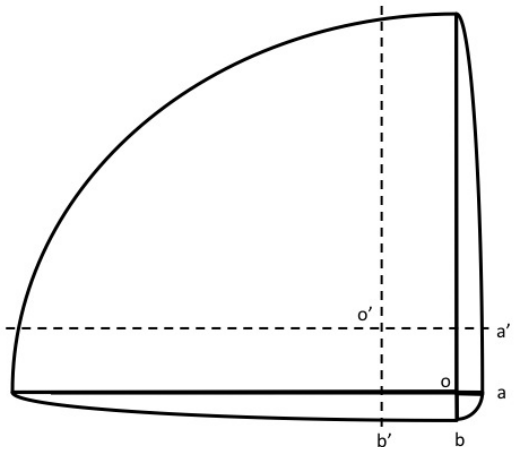

Figure 20: Move the centroid in the principle direction with bad ratio to arrive to normal shape.

3.4 Initial spring configuration connecting two sub-poly-ellipsoids

Our initial model included a certain number of spring elements connecting two sub-poly-ellipsoids as shown in Figure 3, once they are generated by subdivision of an original poly-ellipsoid. These springs will behave like cohesive zones to simulate the fracture processes of the particles. With the constraints of the springs, our particle fracture model may show the three different fracture modes.

3.4.1 Initial spring stiffness

The initial spring stiffness for two sub-poly-ellipsoids are derived based on their Young's moduli, their geometries, and the number of springs on a given break plane. Suppose there are n_s springs in one break plane, the Young's modulus of particles are E, fracture area (area of the break plane) is A, and the centroid-to-centroid distance of the two sub-poly-ellipsoids in the break direction is l, then the initial spring stiffness of springs for this plane is

$$K_0 = \frac{EA}{n_s l} \tag{34}$$

3.4.2 Correction of the Spring Force

Our current simulations are based on the configuration of spring forces between sub-paticles described in the previous sections. Tests are conducted using simple hexagonal close-packed spheres. In analyzing renderings of the particle motion in these simulations, we observed that breakage of springs introduces a noticeable source of new energy into the system, which produces spurious vibrations in the samples. This result suggests that the configuration of springs in these simulations may be incorrect. An analysis of the simulation data showed that spring forces are nonzero when they are broken, thus breakage of spring will cause a sudden change in the loading states of sub-particles.

Recall that breakage parameter D is increased proportional to the crack propagation speed c_f at each step. The fracture propagation speed is on the order of $1\,\mathrm{km\,s^{-1}}$) and the

sand grain diameter is on the order of 0.6 mm, thus crack transit time is on the order of 6×10^{-7} s so that a large decrease in the breakage parameter D, occurs in a single time step. This leads to large oscillations in the spring force, which may produce macroscale vibrations the sample. If we use a virtual smaller fracture propagation speed, then the process of spring breakage will be very long, which is also not reasonable. In consideration of these limitations, we configure the spring force with an alternative method, which is more straightforward.

After the calculation of the initial cohesive force in each spring f_i, the spring force can be calculated as

$$f = f_i - k\Delta d, \tag{35}$$

where k is the stiffness of the spring, and Δd is the elongation in the spring. The spring stiffness is determined by the fracture energy of the sand grain. Figure 21 shows the cohesive law we used for our spring; elongation of spring will decrease the spring force and once the spring force drops to zero, the spring will break irreversibly. The area of under the force-displacement curve for the cohesive law is the work done by spring, which should be equal to the fracture energy $G_c \cdot A$ of the sand grain,

$$\frac{f_i^2}{2k} = G_c \cdot A \tag{36}$$

$$\Rightarrow k = \frac{f_i^2}{2G_c A}, \tag{37}$$

where A is the fracture area for each spring, i.e. the area of the break plane A_{total}/n_s, n_s is number of springs on the break plane, and the cohesive energy G_c can be calculated from fracture toughness K_{Ic} by Irwin's formula [Irwin, 1957] as

$$G_c = \frac{K_{Ic}^2}{E'} \tag{38}$$

where $E' = \frac{E}{1-\nu^2}$. Daphalapurkar et al. [2011] determined from experiment that the fracture toughness is $1.77\, MPa \cdot m^{0.5}$ for the silica sand of the type used in our simulation as well as and others' experimental work [Kabir et al., 2010, Luo et al., 2011, Bari et al., 2012].

3.4.3 Initial cohesive force in the springs

In order to keep the kinematic states of the particles unchanged during subdivision, we need to make sure that the acceleration of sub-particles A and B are the same as that of the original particle O. This can be achieved by applying an initial cohesive force in the springs as described by Morris et al. [2006].

We denote $f_{A/B}$ as the force acting on sub-particle A by sub-particle B, $f_{B/A}$ as the force acting on sub-particle B by sub-particle A. With the help of $f_{A/B}$, the kinematic state of sub-particle A should be kept the same after sub-division, so the equation of motion of sub-particle A is

$$m_A \mathbf{a}_A = \mathbf{F}_A + \mathbf{f}_{A/B} + m_A \mathbf{g} \tag{39}$$

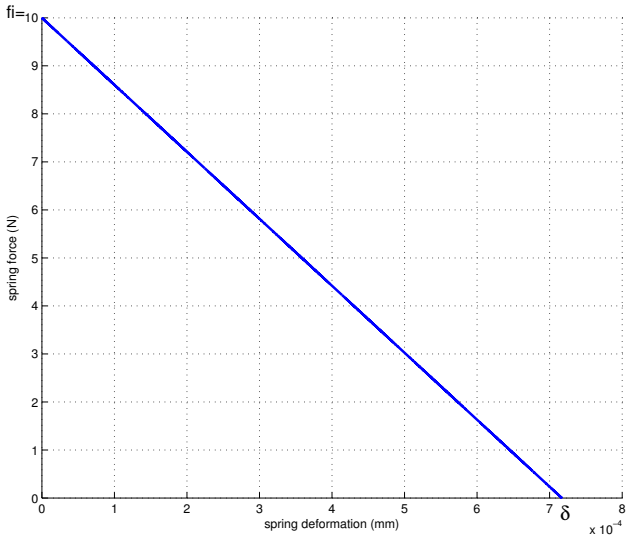

Figure 21: Illustration of the spring force-displacement relationship in the cohesive law. The cohesive law is defined so that the area under the load-displacment curve equals the fracture energy of the sand grain. In this example the initial spring force is $f_i = 10\,\mathrm{N}$, the particle radius is $0.3\,\mathrm{mm}$, and $n_s = 4$; the allowed maximum elongation of the spring is $7.16 \times 10^{-4}\,\mathrm{mm}$ as plotted here.

Where $\mathbf{g}$ is body force, and $\mathbf{F}_A$ the resultant force of all contact forces on sub-particle A. The resultant contact forces on each sub-particle combine to the resultant contact forces on the original particle O, $\mathbf{F}_A + \mathbf{F}_B = \mathbf{F}_O$. From this, we solve for initial cohesive force,

$$\mathbf{f}_{A/B} = \mathbf{F}_A + m_A\mathbf{g} - m_A\mathbf{a}_A \tag{40}$$

$$= \mathbf{F}_A + m_A\mathbf{g} - m_A\mathbf{a}_O. \tag{41}$$

The point of action for $\mathbf{f}_{A/B}$ on sub-particle A is calculated so that the angular acceleration of sub-particle A is kept the same as that of the original particle O, i.e. $\alpha_A = \alpha_O$. And since $\mathbf{f}_{A/B}$ is the resultant force of all the springs on the break plane, the force of each spring can be calculated from $\mathbf{f}_{A/B}$ and the number of springs, n_s.

From Newton's third law, we have in theory that

$$f_{A/B} = -f_{B/A} \tag{42}$$

However, it may not be the case in our fracture model, since the sub-particles may lose some contacts from the original particle as we have described in Section 3.3.1. To correct for this, we calculate $\mathbf{f}_{B/A}$ from the equation of motion of sub-particle B in a consistent manner, with the new cohesive force acting on sub-particle A,

$$\mathbf{f}'_{A/B} = \frac{\mathbf{f}_{A/B} - \mathbf{f}_{B/A}}{2}. \tag{43}$$

4 Simulation of Single Particle Fracture

In order to test our particle fracture model, we compare simulation results for single-particle fracture with an experimental result of the crushing of a single sand grain[2]. In this experiment, a sand particle is placed between two flat platens, and the top platen is moved downward at a constant speed. The sand particles can break under this diametric loading. In order to make the initial state for the simulation and experiment as similar as possible, the particle shape used in the simulation is defined as a poly-ellipsoid fit to Synchronized MicroTomography image of the actual sand particle from the experiment. Figure 22 shows the force-displacement curve for the simulation and experiment of single particle fracture. The first peak of the curve corresponds to the formation of an initial crack through the sand grain, which allows a temporary loss off contact and corresponding drop in the measured force. As the displacement continues, the large fragments are recompressed, causing the force to build to the second peak, which marks the onset of crushing/comminution of the remaining fragments. In order to fit the experiment curve, with emphasis on matching the two peaks in the experiment, we parameterize the model so that sub-division occurs at the first peak, and decohesion of the springs occurs at the second peak.

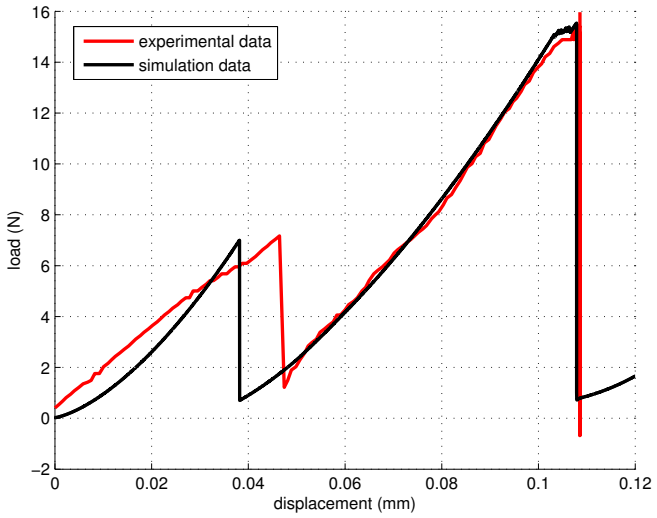

Figure 22: Force-displacement curve for simulation and experiment of single-particle fracture.

There are several sources of uncertainty in the experimental results, and the subsequent model parameterization. (1) As mentioned before, significant differences are apparent in the force-displacement response for similarly shaped Mason sand grains in the experiment, this is attributed to statistical variability in the material strength. (2) From Figure 22, we can see that the top platen experience about 0.11 mm movement before the particle is totally broken, while the diameter of the particle between two platens is only about 0.6 mm. This

[2]the results are one example from numerous tests from unpublished results from Prof. Khalid Alshibli's group at University of Tennessee Knoxville

suggests that there must be some rearrangement (sliding or rolling contact) of the fragments, during the loading process. (3) In order to fit the initial slope of the load displacement curve, it was necessary to define a Young's modulus for the particle of 4 GPa; this value is unrealistically low in comparison with data by Daphalapurkar et al. [2011], who determined that the Young's modulus for silica sand is 41.4 GPato115.8 GPa. (4) There are not enough experiments in order to determine a relationship of material strengths to grain size. Because of these reasons, we decided to use the material strengths in the literature [Hoek and Martin, 2014, Brzesowsky et al., 2011] instead of inferring material strengths from our experimental results.

Besides, we have also done some parameter tests for this single particle test, which is summarized in Table 1. This can tell us that we may use 5×10^{-8} as the time step in our simulation.

Dynamic Simulation		
$\dot{\epsilon}$	$\Delta t\,(s)$	result
10^0	5×10^{-7}	blow up, spring force is too large
10^1	5×10^{-8}	good, same result
10^1	1×10^{-7}	good, same result
10^3	1×10^{-7}	stable, but result is slightly different
10^4	1×10^{-7}	never broken, $d \in [0, 0.12]mm$
10^4	1×10^{-8}	never broken, $d \in [0, 0.12]mm$
Dynamic Relaxation		
$\dot{\epsilon}$	$\Delta t\,(s)$	result
10^{-1}	5×10^{-7}	good
10^1	5×10^{-7}	good, same at $\Delta t = 10^{-1}$
10^3	1×10^{-7}	never broken, $d \in [0, 0.12]mm$
10^3	5×10^{-7}	never broken, $d \in [0, 0.12]mm$

Table 1: Dynamic simulation results. Parameter study for single particle fracture simulations.

5 Numerical results for simulations of Split Hopkinson Pressure Bar experiment at high strain rate

In this section, we will compare the results from our simulations of different initial samples with corresponding experimental results [Kabir et al., 2010, Luo et al., 2011, Bari et al., 2012] in the literature for Split Hopkinson Pressure Bar using silica sand. The SHPB experiment can be idealized as uniaxial compaction at a high strain rate. Thus we can simulate SHPB experiment as a uniaxial compaction using a small RVE. Previous researchers have demonstrated that it doesn't matter whether the RVE is cubic or cylindrical. In this research, we will use a cubic RVE to simulate the SHPB experiment at a strain rate of about $500\,\mathrm{s}^{-1}$. In order to test the effects of different packings, we conduct the same SHPB simulations using 4 different configurations of spherical particles as shown in Figures 23 to 26,

(1) randomly packed, polydisperse spheres, (2) randomly packed monodisperse spheres, (3) hexagonal closed packing of monodisperse spheres, and (4) simple cubic packing of monodisperse spheres. The mechanical properties the of particles in each samples are identical, Young's modulus $E = 60\,\text{GPa}$ [Daphalapurkar et al., 2011], Poisson's ratio $\nu = 0.17$ [Lines], density for silica sand $\rho = 2.65 \times 10^3\,\text{kg}\,\text{m}^{-3}$ [Lines], tensile strength for base size $x_M = 3\,\text{mm}$ is $\sigma_t = 300\,\text{GPa}$ [Brzesowsky et al., 2011], and Weibull's modulus $w = 1$.

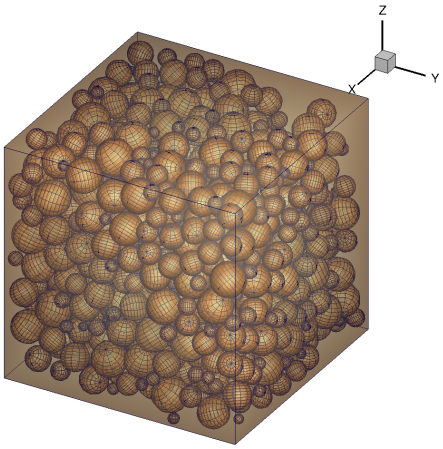

Figure 23: Random packed sample with different sized spheres, mean radius of 0.3 mm.

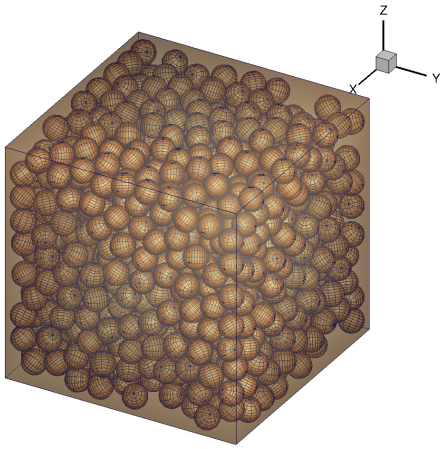

Figure 24: Random packed sample with same sized spheres, radius of 0.3 mm.

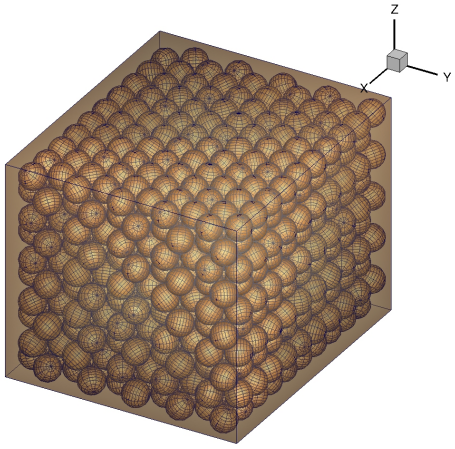

Figure 25: Hexagonal closed packed equal-spheres, radius of 0.3 mm.

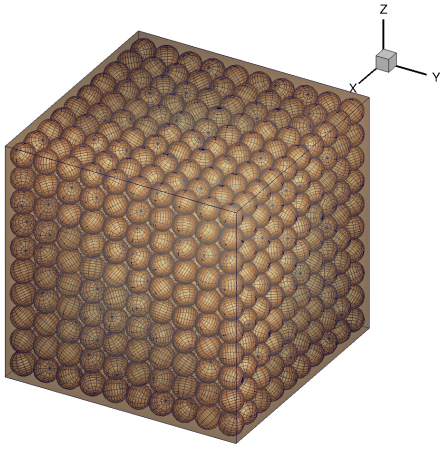

Figure 26: Simple cubic packed equal spheres, radius of 0.3 mm.

5.1 Result for random packed sample with different size

A truncated normal distribution with a mean radius of 0.3 mm, a variance of 0.05 mm, a minimum radius of 0.1 mm, and maximum radius of 0.45 mm is used to generate spherical

particles in the initial sample. Then the sample was packed to 55% packing fraction using a method described in [He et al., 1999]. Note that the orientations of the spheres are randomly distributed after they are settled down. The sample is in a cubic container with dimension of $6\,\mathrm{mm} \times 6\,\mathrm{mm} \times 6\,\mathrm{mm}$ and contains 955 spheres. The top boundary in the z direction is moved downward at a constant strain rate of $500\,\mathrm{s}^{-1}$, the other five boundaries are fixed during the simulation. The simulation results are then compared to SHPB experimental results with silica sand reported in the literature [Kabir et al., 2010, Luo et al., 2011, Bari et al., 2012], as shown in Figure 27. This simulation was conducted with each of the techniques of our particle fracture model, including as cohesive springs, rotation of break planes, random slight rotation of break planes, and with random orientation of the principal directions.

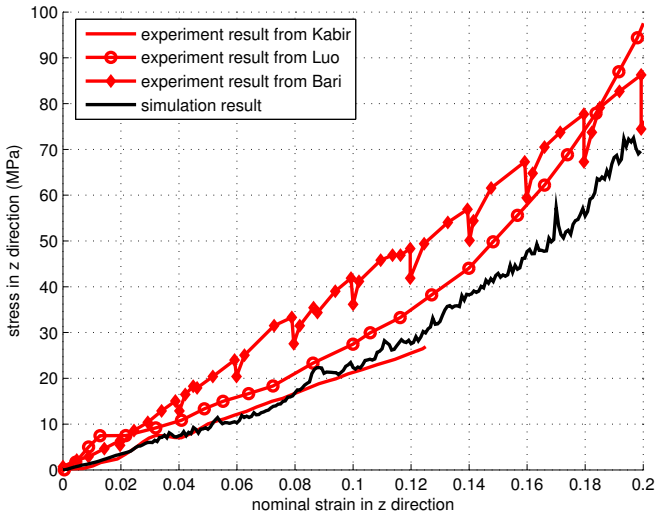

Figure 27: Comparison with experiment results show that our particle fracture model can capture the mechanical behavior very well.

Figure 27 shows that the simulation results lie between those reported by Kabir et al. [2010] and Luo et al. [2011], but are well below the results reported by Bari et al. [2012]. To understand the difference between these results, the characteristics of initial powder bed are summarized in Table 2. Importantly, the aspect ratio of the initial sample H/d of Bari et al. [2012]'s experiment is so large (3.424) that the results may be dominated by the Janssen effect (boundary tractions supporting the majority of the load. In fact we can see this Janssen effect from Fig. 7 in their paper [Bari et al., 2012]. Additionally, Bari et al. [2012] used static loading in their experiment which is different from others [Kabir et al., 2010, Luo et al., 2011] and our simulation. In light of these substantial differences, we don't expect that our simulation results will agree with Bari et al. [2012]'s result. Considering the difference in initial sample size and initial density ρ_0 between the simulations and experiment, and the differences in experimental results from the ostensibly similar experimental investigations, we conclude that our simulations can capture the mechanical behavior of SHPB experiment very well. For comparison, Kabir et al. [2010] showed that even for experiments with nominally identical initial samples, the test-to-test variability produces larger differences than

the difference between our model and the experiment; this variability can be seen in Figure 28.

We need to mention that the strain rate for different experiments and simulation are different as shown in Table 2. However, Kabir et al. [2010], Martin et al. [2013] observed from their experiments that strain rate did not show significant effect in the mechanical behavior over range from $470 \sim 1450\,\mathrm{s}^{-1}$ in Section *strain-rate effect* in [Kabir et al., 2010], and $0 \sim 1000\,\mathrm{s}^{-1}$ in Fig. 24 in [Martin et al., 2013].

	height (H, mm)	diameter/width (d, mm)	H/d	initial density (ρ_0, $\mathrm{g\,cm^{-3}}$)	strain rate ($\dot{\epsilon}$, $\mathrm{s^{-1}}$)
Kabir et al. [2010]	9.3	19.05	0.488	1.50	470
Luo et al. [2011]	10.49	12.70	0.826	1.51	675
Bari et al. [2012]	8.15	2.38	3.424	\	static
our simulation	6	6	1	1.439	500

Table 2: Comparison of initial sample properties from experimental and numerical compaction studies. Bari et al. [2012]'s results are not directly comparable to the others because the value of H/d is so large that Janssen effect will dominate (Janssen effect is already shown in Fig. 7 in their paper [Bari et al., 2012]), and the loading is static (whereas the others are dynamic).

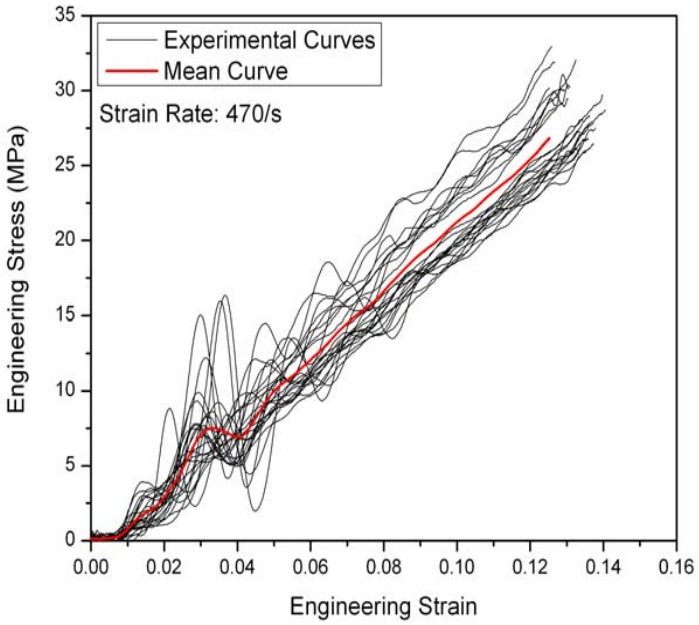

Figure 28: Experimental data for SHPB experiments showing significant variability. The red curve is the mean curve of 26 curves from SHPB experiment using samples with same initial size, initial density, and same type of sand, i.e. silica sand, figure from [Kabir et al., 2010].

Figure 29 shows the sample after the compaction simulation. The size redistributions after compression are shown in Figure 30 and Figure 31 for Kabir et al. [2010]'s experiment

and our simulation, respectively. Both figures show a shift of particle size distribution before and after compression. Figure 31 shows that predictions of particle breakage in the simulation of compaction produce a similar bimodal distribution as the experimental results in Figure 30. Additionally, Figure 31 shows that size appears to converge to a final value with continued loading, which would suggest that either the material is fully dense, or that further communution is prevented by the particle-division constraint.

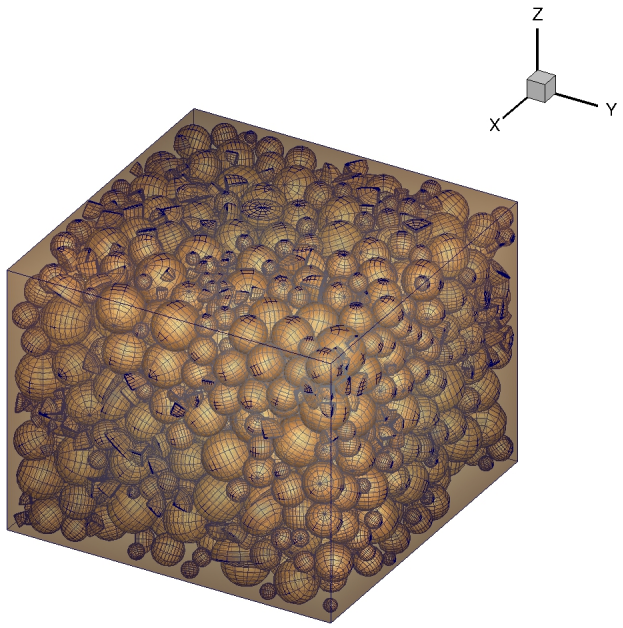

Figure 29: Simulation results showing the post-compaction sample configuration for an initially random-packed sample of uniformly sized spheres.

The difference between the simulation results (Figure 31) and Kabir et al. [2010]'s experiment result (Figure 30) may come from: (1) differences in the initial size distribution, and (2) the limitation that a *normal*-shaped particle can break, at most, only three times; which prevents the formation of very fine particles.

5.1.1 Effect of particle fracture in SHPB simulation

In order to study how much particle fracture can affect the mechanical behavior of a SHPB simulations, and to know whether a particle fracture model is necessary or not in predicting SHPB experiments, we conduct the same uniaxial compression simulation with the same sample and same parameters, but turn off the capability of particle fracture. This result is shown in Figure 32, from which we can see that sample without particle fracture is much stiffer than the samples in experiments. This provides compelling evidence as to the necessity of developing a suitable particle fracture model for DEM simulations of SHPB experiments.

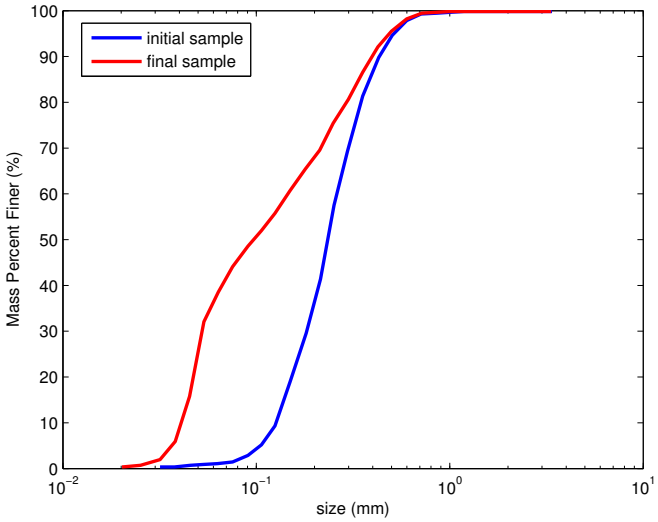

Figure 30: Experimentally measured size distribution for the initial sample and for the sample after a SHPB experiment [Kabir et al., 2010].

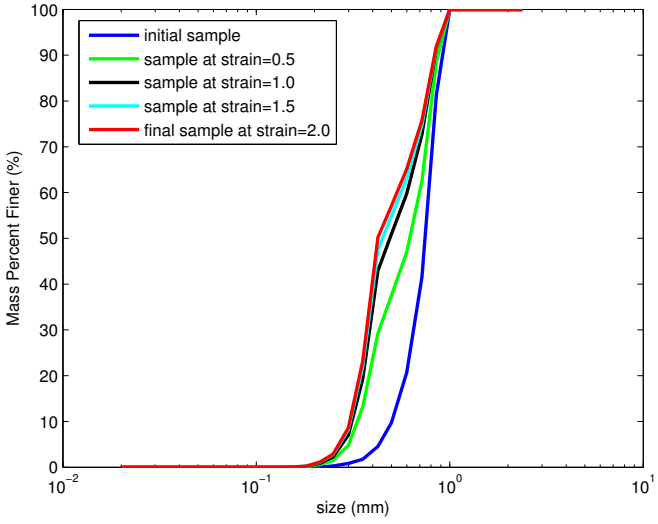

Figure 31: Size distribution for the sample at different strain states from simulation results.

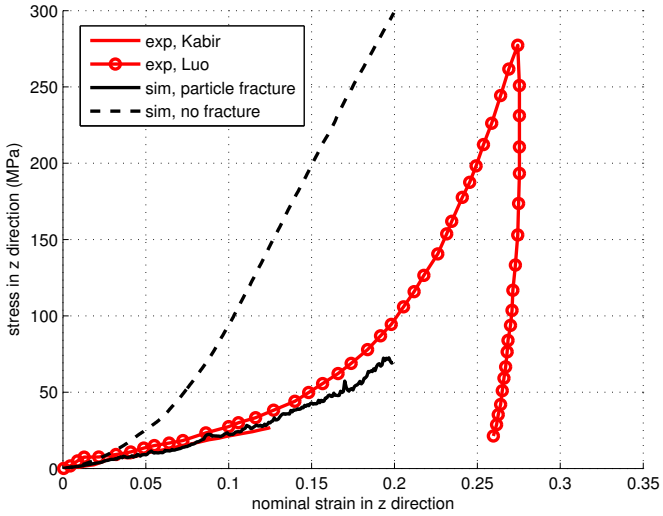

Figure 32: Comparison of the compaction response from experiments and for DEM simulations with and without particle fracture. The simulation without particle fracture shows much stiffer behavior than experiment results, which demonstrates the importance of a particle fracture model in simulating SHPB experiments.

5.1.2 Effects of different techniques in particle fracture model

To improve the overall performance of our particle fracture model by reducing the loss of contacts in splitting we implemented several techniques including ideal break plane rotation, and random slight rotation of the break plane, as described in Section 3.3. Additionally, we would like to see the effects of cohesive springs in our model, and to determine what would happen if we conduct a simulation with the same sample but orienting the principle directions of the spheres in the x, y, z directions as shown in Figure 33 (without rotation of break plane). In such case, most of break planes would be in z direction, leading to contact loss in z direction, which is the compression direction. This test is a worst-case-scenario for loss of contact, and gives an estimate of the magnitude of the error associated with this mechanism.

Figure 34 shows how the choice in simulation technique affects the results. Considering the random variable P we used in Weibull's function of strength, namely Equation (18), it is expected that there will be some difference between different simulations. However, the magnitude of the differences between the simulations are within the differences between experiments such that we can conclude that these additional modifications to the fracture algorithm (cohesive springs, rotation of break plane, and random slight rotation of break plane) do not greatly affect the overall mechanical behavior for this sample of random-packed differently-sized spheres.

This result has important implications to the validity of our approach, indicating that it is not necessary to rotate the principle directions of particles so that they break along the ideal break plane; random orientation of the initial break planes produces a similar effect. This is important because we are not able to arbitrarily rotate the principle directions of ellipsoids

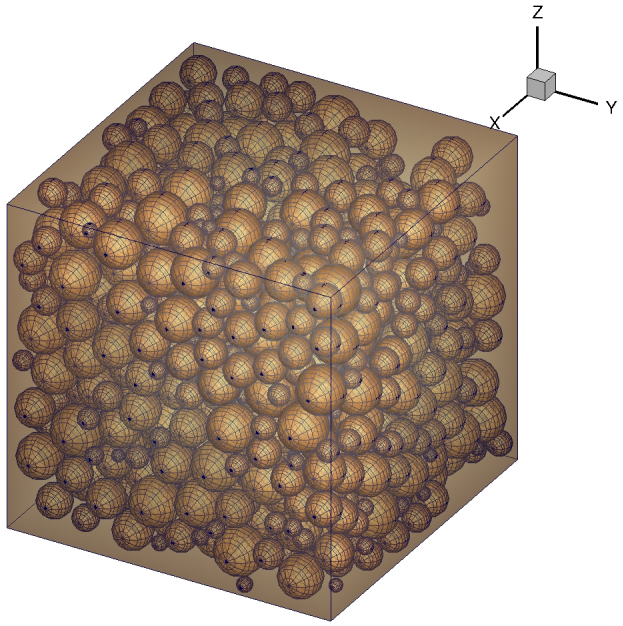

Figure 33: Packed bed with spheres initially oriented in x, y, z directions, such that most of spheres will break in z direction, leading to contact loss in this direction.

and poly-ellipsoids. If instead we oriented spheres in initial sample in x, y, z directions, the response is somewhat softer, which is to our expectation since its most of contact loss happen in the compression direction. Nonetheless, the deviation is within the experimental variability, even for this pathological case.

5.2 Results for different sample packing

Figures 24 to 26 show the effect of different sample packings on the simulated response of SHPB experiments. The radius of spheres in these samples are all 0.3 mm, except for the random-packed sample with different sized spheres, in which the mean radius of spheres is 0.3 mm. There are $10 \times 10 \times 10$ layers of spheres in x, y, z directions in hexagonal closed packed samples and simple cubic packed samples, and 1050 spheres in the sample labeled *randomly-oriented, same-sized* in Figure 24. The differences between the initial samples and their strain-rates are summarized in Table 3. Their different stress-strain curves are compared in Figure 35.

5.2.1 Density effect

As shown in Figure 35 and Table 3, denser samples have much stiffer behavior than looser samples, which is also reported by Kabir et al. [2010], Luo et al. [2011] from their SHPB experiments. Other factors that may influence the behavior of different samples include, (1) larger particles within sample *random, diff*, i.e. Figure 23 where more defects are assumed to exist in a larger particle according to a Weibull function, causing larger particles to break first and then soften the sample, (2) very high coordination number for particles, 12 for

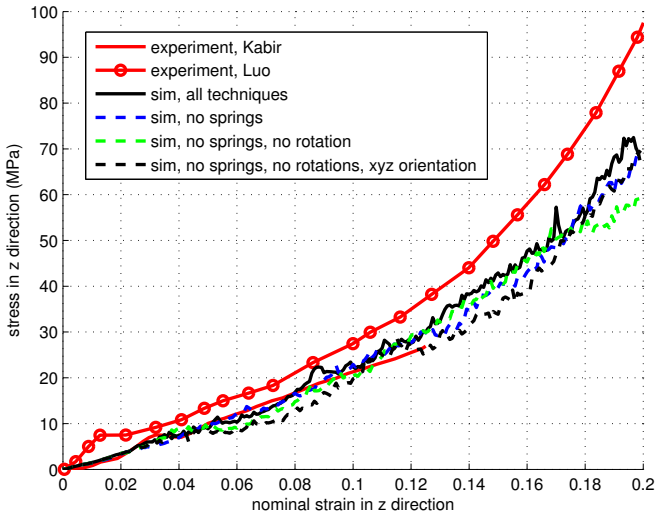

Figure 34: Comparison of the uniaxial compaction response in SHPB experiments and numerical simulations with different model features. The sample with initial x, y, z orientation of potential break planes is somewhat softer, as expected, but the magnitude of the differences between the simulations are within the magnitude of the differences between the experiments, suggesting that these modifications to the model don't critically affect results for this sample type.

	height (H, mm)	diameter/width (d, mm)	H/d	initial density (ρ_0, g/cm^3)	strain rate ($\dot{\epsilon}$, $1/s$)
cubic packing (Figure 26)	6	6	1	1.388	500
random, diff (Figure 23)	6	6	1	1.439	500
random, same (Figure 24)	6	6	1	1.457	500
hex packing (Figure 25)	5.009	6.300/5.450	0.795/0.919	1.743	499

Table 3: Simulation parameters to investigate effects of sample packing and density.

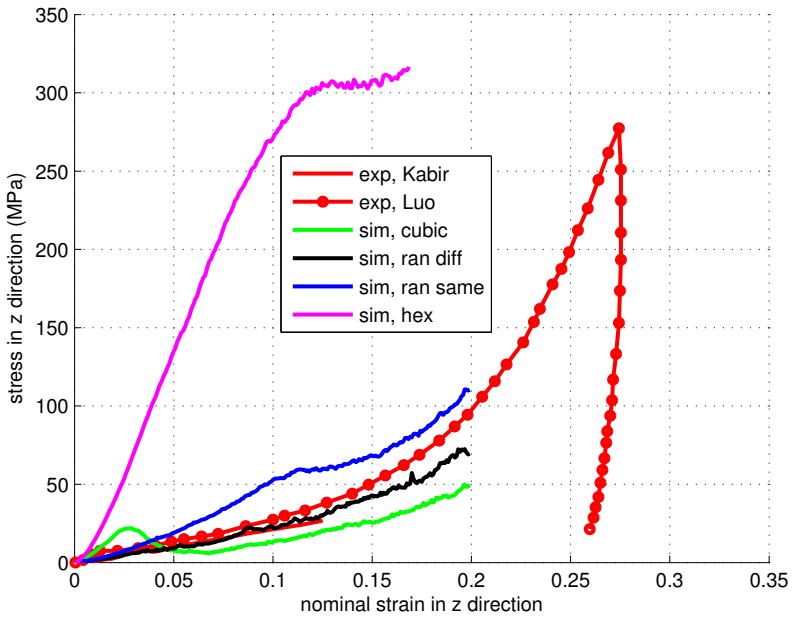

Figure 35: Comparison of the uniaxial compaction response in SHPB experiments and numerical simulations showing the effect of packing type. Denser samples with a structured packing are much stiffer than looser samples, which is also observed by Kabir et al. [2010], Luo et al. [2011] from experiments.

hexagonal packed sample in Figure 25 make particles hard to break, which is consistent with observations from experiments [Lade et al., 1996, Tsoungui et al., 1999, Nakata et al., 2001, Vilhar et al., 2013], and (3) simple cubic packed sample in Figure 26 is very regular, which makes it stiff at beginning since all the particles are utilized to sustain the compressive loading in z direction. Then after many particles break, there are fewer particles that can sustain the compressive loading, which makes the sample softer.

5.2.2 Sample aspect ratio effect

In order to study the effect of the aspect ratio of samples on their mechanical behavior (*i.e.,* the boundary effects), we generated $10 \times 10 \times 7$ layers of spheres in a hexagonal closed packed sample and a simple cubic packed sample as summarized in Table 4. The results are plotted in Figure 36, which shows a boundary effect for the shorter samples.

6 Conclusions

We developed an adaptive particle fracture model in poly-ellipsoidal DEM. In our particle fracture model, poly-ellipsoidal particles will be first sub-divided into several sub-poly-ellipsoids by external loadings based on Hoek-Brown fracture criterion and the maximum tensile stress in contacts. Initially these sub-poly-ellipsoids are bonded by cohesive springs, and further loadings will finally break the particle by breaking these cohesive springs. In

Packing Type	height (H, mm)	dia./width (d, mm)	H/d	initial density (ρ_0, g/cm^3)	strain rate ($\dot{\epsilon}$, $1/s$)
hex, short	3.540	6.300/5.450	0.562/0.650	1.726	500
hex (Figure 25)	5.009	6.300/5.450	0.795/0.919	1.743	500
cubic, short	6	6	1	1.388	500
cubic (Figure 26)	4.2	6	0.7	1.388	500

Table 4: Simulation parameters to investigate effects of sample aspect ratio, which correlates to boundary effects.

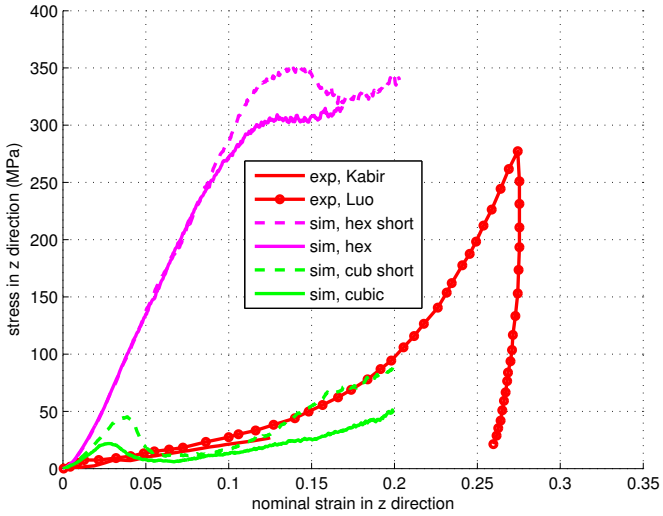

Figure 36: Comparison of the uniaxial compaction response in SHPB experiments and numerical simulations showing the effect of sample aspect ratio. Shorter samples are stiffer, indicating the influence of boundary effects.

order to approximate better the original shape of poly-ellipsoid by sub-poly-ellipsoids, we tried numerical techniques, such as ideal break plane rotation, and random slight rotation of the break plane, as described in Section 3.3. Also, we considered the statistics and size effects on particle strengths using Weibull theory.

In numerical examples, we simulated high strain-rate split Hopkinson pressure bar experiments of silica sand. (1) The results showed that our particle fracture model can capture the mechanical behavior of these experiments very well. (2) Also we showed by numerical example that particle fracture model is very necessary in studies of dynamic behavior of sand grains. Otherwise, the numerical model will virtually stiffen the sand samples. (3) Besides, numerical results showed that the two numerical techniques, i.e. ideal break plane rotation, and random slight rotation of the break plane, have little effects in our model. It means that these techniques are not necessary and can be turned off in simulations. (4) Finally, the effects of density and packing of sand sample are studied numerically. And we observed the same behavior as reported by Kabir et al. [2010], Luo et al. [2011] from their SHPB experiments, i.e. denser samples are much stiffer than looser samples. Difference in packing will cause the difference in coordination number of particles in the samples, our numerical examples also showed that sample with higher coordination number, such as hexagonal close packing, is much stiffer, which is consistent with observations from experiments [Lade et al., 1996, Tsoungui et al., 1999, Nakata et al., 2001, Vilhar et al., 2013].

References

J. E. Andrade, I. Vlahinić, K.-W. Lim, and A. Jerves. Multiscale 'tomography-to-simulation' framework for granular matter: the road ahead. *Géotechnique Letters*, 2:135–139, 2012.

D. André, M. Jebahi, I. Iordanoff, J.-L. Charles, and J. Néauport. Using the discrete element method to simulate brittle fracture in the indentation of a silica glass with a blunt indenter. *Computer Methods in Applied Mechanics and Engineering*, 265:136–147, 2013.

JA Åström and HJ Herrmann. Fragmentation of grains in a two-dimensional packing. *The European Physical Journal B-Condensed Matter and Complex Systems*, 5(3):551–554, 1998.

P Bari, H Bale, and JC Hanan. Observing 3-d deformation of silica sand under in-situ quasi-static compression. *Mechanics of Materials*, 54:84–90, 2012.

O Ben-Nun, I Einav, and A Tordesillas. Force attractor in confined comminution of granular materials. *Physical review letters*, 104(10):108001, 2010.

Oded Ben-Nun and Itai Einav. The role of self-organization during confined comminution of granular materials. *Philosophical Transactions of the Royal Society of London A: Mathematical, Physical and Engineering Sciences*, 368(1910):231–247, 2010.

RH Brzesowsky, CJ Spiers, CJ Peach, and SJT Hangx. Failure behavior of single sand grains: Theory versus experiment. *Journal of Geophysical Research: Solid Earth (1978–2012)*, 116 (B6), 2011.

Y. P. Cheng, Y. Nakata, and M. D. Bolton. Discrete element simulation of crushable soil. *Géotechnique*, 53:633–641, 2003.

Gye-Chun Cho, Jake Dodds, and J Carlos Santamarina. Particle shape effects on packing density, stiffness, and strength: natural and crushed sands. *Journal of Geotechnical and Geoenvironmental Engineering*, 132(5):591–602, 2006.

MB Cil and KA Alshibli. 3d assessment of fracture of sand particles using discrete element method. *Géotechnique Letters*, 2(July-September):161–166, 2012.

P. A. Cundall and O. D. L. Strack. A discrete numerical model for granular assemblies. *Géotechnique*, 29:47–65, 1979.

P.A. Cundall and R.D. Hart. Development of generalized 2-d and 3-d distinct element programs for modeling jointed rock. Technical report, DTIC Document, 1985.

NP Daphalapurkar, F Wang, B Fu, H Lu, and R Komanduri. Determination of mechanical properties of sand grains by nanoindentation. *Experimental Mechanics*, 51(5):719–728, 2011.

JJ Gallagher, M Friedman, J Handin, and GM Sowers. Experimental studies relating to microfracture in sandstone. *Tectonophysics*, 21(3):203–247, 1974.

John J Gallagher Jr et al. Fracturing of quartz sand grains. In *The 17th US Symposium on Rock Mechanics (USRMS)*. American Rock Mechanics Association, 1976.

Jim Guilkey, Todd Harman, Justin Luitjens, John Schmidt, Jeremy Thornock, JD de St Germain, Siddharth Shankar, Joseph Peterson, Carson Brownlee, C Reid, et al. Uintah user guide. Technical report, SCI Institute Technical Report, 2009.

Bobby O Hardin. Crushing of soil particles. *Journal of Geotechnical Engineering*, 111(10): 1177–1192, 1985.

D. He, N.N. Ekere, and L. Cai. Computer simulation of random packing of unequal particles. *Physical Review. E*, 60(6):7098, December 1999.

E Hoek and CD Martin. Fracture initiation and propagation in intact rock–a review. *Journal of Rock Mechanics and Geotechnical Engineering*, 6(4):287–300, 2014.

M.A. Hopkins. Discrete element modeling with dilated particles. *Eng. Comp.*, 21:422–430, 2004.

Mark A. Hopkins. Polyhedral on the cheap. *DEM5-2010*, 2010.

David A Horner, John F Peters, and Alex Carrillo. Large scale discrete element modeling of vehicle-soil interaction. *Journal of engineering mechanics*, 127(10):1027–1032, 2001.

E.S. Hosseininia and A.A. Mirghasemi. Numerical simulation of breakage of two-dimensional polygon-shaped particles using discrete element method. *Powder Technology*, 166(2):100–112, 2006.

GR Irwin. Analysis of stresses and strains near the end of a crack traversing a plate. *J. Appl. Mech.*, 1957.

Md E Kabir, Bo Song, Bradley E Martin, and Wayne Chen. Compressive behavior of fine sand. *Albuquerque, NM*, 2010.

M.A. Knuth, J.B. Johnson, M.A. Hopkins, R.J. Sullivan, and J.M. Moore. Discrete element modeling of a Mars Exploration Rover wheel in granular material. *Journal of Terramechanics*, 49:27–36, 2012.

Poul V Lade, Jerry A Yamamuro, and Paul A Bopp. Significance of particle crushing in granular materials. *Journal of Geotechnical Engineering*, 122(4):309–316, 1996.

Hengxing Lan, C Derek Martin, and Bo Hu. Effect of heterogeneity of brittle rock on micromechanical extensile behavior during compression loading. *Journal of Geophysical Research: Solid Earth (1978–2012)*, 115(B1), 2010.

Murray Lines. Silica - silicon dioxide (sio2). `www.azom.com/article.aspx?ArticleID=1114`.

H Luo, H Lu, WL Cooper, and R Komanduri. Effect of mass density on the compressive behavior of dry sand under confinement at high strain rates. *Experimental mechanics*, 51 (9):1499–1510, 2011.

Huiyang Luo, William L Cooper, and Hongbing Lu. Effect of moisture on the compressive behavior of dense eglin sand under confinement at high strain rates. In *Dynamic Behavior of Materials, Volume 1*, pages 381–388. Springer, 2014a.

Huiyang Luo, William L Cooper, and Hongbing Lu. Effects of particle size and moisture on the compressive behavior of dense eglin sand under confinement at high strain rates. *International Journal of Impact Engineering*, 65:40–55, 2014b.

BE Martin, Md E Kabir, and W Chen. Undrained high-pressure and high strain-rate response of dry sand under triaxial loading. *International journal of impact engineering*, 54:51–63, 2013.

Wolfram MathWorld. Rotation matrix. `mathworld.wolfram.com/RotationMatrix.html`.

Glenn R McDowell and John P de Bono. On the micro mechanics of one-dimensional normal compression. *Géotechnique*, 63, 2013.

RD Mindlin. Compliance of elastic bodies in contact. *Journal of applied mechanics*, 16(3): 259–268, 1949.

Joseph P Morris, MB Rubin, GI Block, and MP Bonner. Simulations of fracture and fragmentation of geologic materials using combined fem/dem analysis. *International Journal of Impact Engineering*, 33(1):463–473, 2006.

Yukio Nakata, Masayuki Hyodo, Adrian Hyde, Yoshinori Kato, and Hidekazu Murata. Microscopic particle crushing of sand subjected to high pressure one-dimensional compression. *Soils and Foundations*, 41(1):69–82, 2001.

E.G. Nezami, Y.M.A. Hashash, D. Zhao, and J. Ghaboussi. A fast contact detection algorithm for 3-D discrete element method. *Comput. Geotech.*, 31:575–587, 2004.

C. O'Sullivan. Particle-based discrete element modeling: geomechanics perspective. *International Journal of Geomechanics*, 11(6):449–464, 2011.

J.F. Peters, M.A. Hopkins, R. Kala, and R.E. Wahl. A poly-ellipsoid particle for non-shperical discrete element method. *Eng. Comp.*, 26:645–657, 2009.

A.V. Potapov and C.S. Campbell. Computer simulation of impact-induced particle breakage. *Powder Technology*, 81:207–216, 1994.

A. Refahi, J. Aghazadeh Mohandesi, and B Rezai. Discrete element modeling for predicting breakage behavior and fracture energy of a single particle in a jaw crusher. *International Journal of Mineral Processing*, 94(1):83–91, 2010.

Richard Regueiro, Ronald Pak, John McCartney, Stein Sture, Beichuan Yan, Zheng Duan, Jenna Svoboda, WoongJu Mun, Oleg Vasilyev, Nurlybek Kasimov, et al. Onr muri project on soil blast modeling and simulation. In *Dynamic Behavior of Materials, Volume 1*, pages 341–353. Springer, 2014.

D. Robertson and M.D. Bolton. Dem simulations of crushable grains and soils. *Powders and grains. Lisse. The Netherlands: Balkema*, pages 623–6, 2001.

AD Salman and DA Gorham. The fracture of glass spheres. *Powder technology*, 107(1): 179–185, 2000.

J.N. Goodier S.P. Timoshenko. *Theory of Elasticity. (third edition)*. McGraw-Hill Book Company, New York, 1970.

OE Strack, RB Leavy, and RM Brannon. Aleatory uncertainty and scale effects in computational damage models for failure and fragmentation. *International Journal for Numerical Methods in Engineering*, 102(3-4):468–495, 2015.

Olivier Tsoungui, Denis Vallet, and JEAN-Claude Charmet. Numerical model of crushing of grains inside two-dimensional granular materials. *Powder technology*, 105(1):190–198, 1999.

Aleksandar S Vesic and G Wayne Clough. Behavior of granular materials under high stresses. *Journal of Soil Mechanics & Foundations Div*, 1968.

G Vilhar, V Jovičić, and Matthew Richard Coop. The role of particle breakage in the mechanics of a non-plastic silty sand. *Soils and Foundations*, 53(1):91–104, 2013.

W Weibull. A statistical distribution function of wide applicability, presented to the american society of mechanical engineers. *Atlantic City, NJ*, 23:981–997, 1951.

C. Wellmann, C. Lillie, and P. Wriggers. A contact detection algorithm for superellipsoids based on the common-normal concept. *Eng. Comp.*, 25:432–442, 2008.

Christian Wellmann and Peter Wriggers. A two-scale model of granular materials. *Computer Methods in Applied Mechanics and Engineering*, 205:46–58, 2012.

Jerry A Yamamuro, Paul A Bopp, and Poul V Lade. One-dimensional compression of sands at high pressures. *Journal of Geotechnical Engineering*, 122(2):147–154, 1996.

B. Yan, R.A. Regueiro, and S. Sture. Three-dimensional ellipsoidal discrete element modeling of granular materials and its coupling with finite element facets. *Eng. Comp.*, 27(4):519–550, 2010.

HP Zhu, ZY Zhou, RY Yang, and AB Yu. Discrete particle simulation of particulate systems: a review of major applications and findings. *Chemical Engineering Science*, 63(23):5728–5770, 2008.